The importance of infragravity waves in the cross-shore sediment transport in the surf zone of a barred intertidal beach

J. W. Stefan Verschure BSc
Student number: 3288811
March 4, 2014

Master Thesis
Department of Physical Geography
Faculty of Geosciences
Utrecht University

Supervisor:
Prof. Dr. B. G. Ruessink

Universiteit Utrecht

Faculty of Geosciences

Abstract

Knowledge about the sediment transport processes active in the intertidal zone is incomplete. Especially the role of infragravity waves, waves with a period of 20-200 seconds, remains unclear. Many authors propose mechanisms by which infragravity waves cause suspended sediment transport in the surf zone. Most mechanisms are based on only small data sets and the resulting suspended sediment transport varies in directions and magnitude. A field campaign of five weeks at the beach of Egmond aan Zee, The Netherlands, was performed to analyse the suspended sediment transport by infragravity waves in the surf zone. 384 bursts of 30 minutes were selected for analysis. The Importance of infragravity waves was strongly related to the normalized location within the surf zone strongly. The normalized location within surf zone was also used to explain the suspended sediment transport by infragravity waves. The infragravity wave suspended sediment transport was comparable in magnitude with the landward directed gravity wave suspended sediment transport. In most of the surf zone seaward directed mean suspended sediment transport component was dominant. It is proved that multiple infragravity wave suspended sediment transport mechanisms were active in the surf zone. A unifying theory of infragravity suspended sediment transport as a function normalized location within surf zone is proposed.

Inhoud

1 Introduction

Coastal erosion has become a growing concern and engineering challenge over the years and will be for the coming decades. Especially considering predicted accelerated sea level rise and the increased likelihood of storm events associated with of global climate change. The most dynamic and morphologically active region at a time scale of a few seconds to several decades is the intertidal zone. However knowledge about the sediment transport processes active in this region is incomplete. Improved understanding of all hydrodynamic processes, associated sand transport and morphological change is essential to accurately solve current and future coastal engineering problems. The intertidal area can be divided into three morphodynamic zones, all associated with different characteristic hydrodynamic and sediment transport processes (Masselink, 1993; Price and Ruessink, 2008): the shoaling zone, the surf zone and the swash zone (from most seaward to most landward). The shoaling zone is the part of the intertidal zone where incident gravity waves shoal until the largest incident waves start to break. The next zone termed surf zone or the transition zone, can be subdivided into the outer surf zone (breaker zone) and the inner surf zone. The outer surf zone is the zone where gravity waves are breaking and the inner surf zone is the zone where all gravity waves are transformed into bores. The swash zone is the part of the intertidal zone that positioned landward of the surf zone. The focus of this MSc Thesis will be on the surf zone.

The surf zone is the most dynamic region in the near shore area considering suspended sediment transport (SST). For accurate predictions of beach change, it is very important to gain knowledge about the processes taking place in the surf zone and the contribution of these processes to sediment transport under different hydrodynamic conditions. Beside gravity waves and currents, IG (IG) waves also influence the SST (Alsina and Cáceres, 2011; Aagaard and Greenwood, 2008; Smith, 2002; Smith and Mocke, 2002; Symonds et al., 1982; Baldock et al., 2011). IG waves have frequencies between 0.005-0.05Hz, higher frequencies than gravity waves (0.05-1Hz). These long IG waves often do not break like gravity waves and are reflected from the coast resulting in a standing or partly standing wave pattern. Especially under storm conditions waves, IG waves may contribute significantly to sediment transport (Russel, 1993).

Already in the 1990s the role of IG waves in cross-shore transport and morphology was recognized (Beach and Sternberg ,1988; Aagaard and Greenwood, 1994; Aagaard and Greenwood, 1995a). However the transport in the surf zone appeared to be spatially and temporally variable both in magnitude and direction (Greenwood, 1995a;

It is therefore not surprising most models concerning cross-shore sediment transport in the nineties were fairly inaccurate in explaining morphological evolution of coastal profiles, especially in the surf and swash zones (Roelvink and Brøker, 1993; Schoonees and Theron, 1995; Aagaard et al., 2002). Schoonees and Theron (1995) compared 10 different model of which only one accurately predicted the wave height associated with IG waves. Roelvink and Brøker (1993) investigated the accurateness of five models and found among other issues that the influence of IG waves on the total sediment transport could increase the performance of the models (3 models did not even include IG waves). One important reason for this lack of inaccuracy, is the lack of knowledge of the processes concerning SST in the surf zone (Roelvink and Brøker, 1993; Aagaard et al., 2002). Another reason models concerning cross-shore sediment transport are fairly inaccurate in explaining morphological evolution of coastal profiles, is because in the surf zone different transport mechanisms interact (Roelvink and Brøker, 1993). Even at the present day there is no model capable of modeling the effect of IG on the sediment transport in the complete intertidal zone.

This thesis will focus on the importance of IG waves to cross-shore sediment transport in the surf zone of a barred intertidal beach. Many authors recognized mechanisms contributing to the cross-shore SST by IG waves in the surf zone. In addition to the literature reviewing a 5-week field experiment was conducted on the beach of Egmond aan Zee, The Netherlands. Hydrodynamics, morphology and cross-shore sediment transport was measured in a cross-shore profile.

In chapter 2 first the hydrodynamics of IG waves, the suspension of sediment and the IG wave SST mechanisms provided in literature are explained. At the end of chapter 2 the hypotheses lead to the following research questions: How does the relative importance of infragravity compared to gravity waves relate to cross-shore location within the surf zone, offshore wave height and water depth? How does the suspended sediment transport by infragravity waves relate to the cross-shore location in the surf zone? Which mechanisms are most likely responsible for the infragravity wave suspended transport pattern in the surf zone? In chapter 3 the research methods are explained, including; the field site, data collection, data screening and data processing. In chapter 4 the boundary conditions and morphological evolution are described and research question 1 and 2 are answered. In the chapter 5, the used method is discussed and research question 3 is answered by proposing a unifying theory of infragravity suspended sediment transport as a function normalized location within surf zone. The most important conclusions are stated in chapter 6.

2 Cross-shore suspended sediment transport by infragravity waves in the surf zone

Many authors recognized mechanisms contributing to the cross-shore SST by IG waves in the surf zone. In order to explain these mechanism both the suspension of sediment and the hydrodynamic conditions in the surf zone are discussed. The hydrodynamic conditions especially the net effect of mean-velocity and oscillatory velocity during suspension and a few seconds after the suspension of sediment determine the net SST.

2.2 Infragravity waves in the surf zone

IG waves, first observed by Munk (1949), often exist in combination with wind generated sea and swell waves. Unlike gravity waves, IG waves are not directly forced by wind. Longuet-Higgins and Stewart (1962) were the first to identify the formation process of IG waves, through the radiation stress gradients between waves with small amplitudes and waves with large amplitudes in wave groups. Considering a simple case of two sets of linear waves (wave trains) with small differences in wave length and equal amplitude, present at the same time on a plane bed, these two wave trains will interfere and produce a single non-linear second order wave. As waves propagate through water they make individual water particles perform an orbital motion. So these changes in velocity cause the waves to exert a momentum (mass multiplied by velocity) and thus a net force on the water. According to the second law of newton the total force applied on a body is equal to the time derivative of the momentum of a body. Consistent with this law the derivative of the momentum is non-zero when the moment changes direction. So even in orbital motion of a linear wave where there is no difference in the magnitude of the velocity for every particle, the derivative is non-zero. Integrated over depth and thus averaged over phase this means linear waves do exert momentum on the fluid but no change of momentum can be observed over time and therefore no net force is exerted on the water body. The depth integrated momentum flux exerted by gravity surface waves on the mean current was defined by Longuet-Higgins and Stewart (1962) as radiation stress. The amplitude varies within the wave group.

Larger waves imply lager orbital velocities and therefore larger radiation stresses. For a closed system with no external forcing and no change of mass, conservation of momentum holds. So the increase of radiation stress due to the presence of non-linear wave groups has to be compensated by another parameter which decreases the radiation stress. The radiation stress in the cross-shore direction (Sxx) is defined as:

$$S_{xx} = \int_{-h}^{\eta}(p + p\tilde{u}^2)dz - \frac{1}{2}\rho g(h - \bar{\eta}), \tag{1}$$

where the integral term is the oscillatory part, pressure is given by p(x,z,t), oscillatory velocity is given ũ(x,z,t). The term (p+pũ2) is integrated over water column. The vertical distance from the bed level to the water surface is z. Making the lower boundary of the integral the bed level z=-h and the upper boundary of the integral the water surface elevation η(x,t). The negative term of the formula in the hydrostatic part, where ϱ is fluid density, g is the gravitational force, h is the water depth and $\bar{\eta}$ the phase averaged water surface elevation. In The cross-shore radiation stress formula water depth, pressure, density and gravitational force can be considered constants for a homogeneous fluid over and horizontal bottom. Only the oscillatory velocity in the oscillatory part and the phase averaged water surface elevation in the hydrostatic part are variables.In the case of random waves along a non-linear profile waves with different wave lengths and wave forms, random waves will interfere and produce a signal of subsequently waves with smaller and larger amplitudes called wave groups. Variation in radiation stress due to the variation in orbital velocities of waves in wave groups leads to radiation stress gradients along a wave group. Subsequently the only other variable in the cross-shore radiation stress formula, water surface elevation, changes accordingly. High waves in the wave group force the water surface elevation to go down while small waves cause higher water surface elevation. As a result a IG wave with the same period and velocity as the wave group propagates with the gravity wave group. Longuet-Higgins and Stewart formulated the cross-shore radiation stress formula in a series of papers from 1960-1964. Longuet-Higgins and Stewart (1964) also suggest explained the forced IG waves by cross-shore radiation stress formula. They also observed that in the breaker zone, where gravity waves start breaking and bound IG waves are released into the surf zone.

An alternative for the generation of IG wave generation was later proposed by Symonds et al. (1982). Symonds et al. (1982) where the first to investigate the effect of changing conditions at breakpoint of incident waves on long wave forcing. Most models before used to explain long waves in the surf zone used constant breaking points and a local water depth dependent breaker amplitude, excluding the effect existing wave groups at breaking point on long waves.

Symonds et al. (1982) made a two-dimensional wave model including a time-dependent non-steady breaking point based on incoming wave groups with different waves of varying breaking point. They found that shoreward of the breaking zone a standing wave pattern existed. Seaward also progressive free waves were observed. This is in agreement with observations of Tucker (1950) and the suggestions of Longuet-Higgins and Stewart (1964). Dong et al. (2009) studied the generation of IG waves by six series of bichromatic wave groups on a steep slope (1:10) and a mild slope (1:40). Breakpoint forced IG waves were observed primarily on the steep slope, while released bound IG waves originally forced by wave groups contributed the most to free IG waves on the mild slope.

These long IG waves often do not break like gravity waves and are reflected from the coast resulting in a standing or partly standing wave pattern. As soon as gravity waves start breaking when moving onshore the relative importance of IG starts to increase (Beach & Sternberg, 1988; Thomsen, 2006). Short wave energy can be transferred to IG waves at the breaking point or bound IG waves become free IG waves when the forcing mechanism, gravity waves, dissipate. The wave height of bound infragravity waves at surf zone boundary, depends on incident waves height. Offshore at a water depth of about 15m the IG wave energy is about 10% of the total wave energy, resulting in maximum IG wave heights of about 0.5m (Munk, 1949; Tucker, 1950; Okihiro et al., 1992). Close to shore IG wave energy can become about 50% of the total wave energy leading to a wave height of about 1m (Beach & Sternberg ,1988; Thomsen, 2006). Where Beach & Sternberg (1988) showed that in the surf zone during high energy conditions (offshore wave height of 3-5m) the oscillatory velocity and SSE variance were explained for 85% and 66% by the IG spectrum respectively. Individual IG waves even reached a amplitude of 1.8 m.

2.2 Suspension of sediment in the surf zone

Initiation of motion of sediment grains is realized when the bed shear-stress stress exerted by the fluid on the grains is larger than the critical bed shear-stress. Once the initiation of motion is generated particles can be transported as bed load transport or suspended load transport. Bed load transport is considered to be the transport of particles due to rolling and sliding or by the means of saltation. Suspended load transport is the transport of particles in suspension. When the bed-shear stress just exceeds the critical value for initiation of motion, a particle will move by the means of rolling and sliding. Higher bed-shear stress values will cause movement by saltation.

For even higher bed-shear stresses vertical fluid velocity exceeds the terminal fall velocity. The particle will go into suspension. The terminal fall velocity is the velocity for which the forces exerted by the fluid in the vertical direction (lift and upward turbulent forces) are the same as the gravitational forces. Bed load transport is, by definition restricted very close to the bed. At 5 mm above the bed SST is of equal magnitude compared to the bed load sediment transport (Bagnold, 1956 cit. Voulgaris and Collins, 2000). At 1 cm above the bed SST usually is some 20 times larger than the bed load transport (Bagnold, 1956 cit. Voulgaris and Collins, 2000). Ruessink et al. (1998) and Osborne and Greenwood (1992) also suggested the contribution of bed load transport compared to the total transport in the surf zone is small. It is therefore safe to assume that the SST is accurately representing the total sediment transport in the surf zone.

In the shoaling zone sediment suspension is initiated by the orbital motion of gravity waves (Yu et al., 1993; Ruessink et al., 1998; Voulgaris and Collins, 2000; Deigaard et al.,1999). High sediment concentrations are restricted to the first few centimeter above the bed (Yu et al., 1993; Smith and Mocke, 2002). When bed-shear stresses in the boundary layer exceed critical bed-shear stress small traveling vortices and turbulent diffusion causes enough bed shear stress to lift sediment out of the boundary layer (Voulgaris and Collins, 2000).

Many investigations show that in the surf zone, peaks in the sediment concentrations over time are related to breaking waves (Alsina and Cáceres, 2011; Aagaard and Greenwood, 2008; Smith and Mocke, 2002; Yu et al., 1993; Voulgaris and Collins, 2000; Aagaard and Hughes, 2010). Yu et al. (1993) and Longo et al. (2002) indicated that major eddies and vortices form after the breaking of gravity waves.

After breaking orbital motions under the short wave crests decrease and the velocity field is completely dominated by turbulence associated with these vortices (Yu et al., 1993; Longo et al., 2002). Vortices are associated with large vertical velocity oscillations which will generate enough bed-shear stress to initiate sediment suspension (Yu et al. 1993; Aagaard and Greenwood, 2008). So in the surf zone when gravity waves start breaking, the orbital velocities of gravity waves as stirring mechanism loses its importance compared to sediment suspension by the turbulence of breaking gravity waves.

Especially when waves are plunging and the relative wave height is large, turbulence induced bed-shear stress can contribute significantly to the total bed-shear stress and therefore to sediment suspension (Yu et al., 1993; Longo et al. 2002). Under plunging waves large vortices are generated rotating clockwise about a horizontal axis parallel to the wave crest (Longo et al., 2002; Aagaard and Hughes, 2010). Plunging waves suspend multiple times more sediment than spilling waves and bores (Beach and Sternberg, 1999; Voulgaris and Collins, 2000; Aagaard and Greenwood, 2008; Aagaard and Hughes 2010) Sediment suspension by breaking of waves causes not only large sediment concentration in the boundary layer but also higher into the water column (Yu et al. 1993). The vertical velocity associated with eddies is intense enough to transport sediment even above the boundary layer (Yu et al., 1993). Furthermore the eddy motions entrain sediment directly from the bed releasing a significant amounts of bubbles which promote mixing an suspension higher into the water column (Yu et al., 1993; Voulgaris and Collins, 2000; Aagaard and Hughes, 2010).

Smith and Mocke (2002) investigated transport in the surf zone. They used two flume experiments under different conditions and a small field survey in a low energetic (Hrms of 0.98m water level at measuring point 1.8 m at high tide and 1.1m at low tide) and mildly sloping (1:40) beach. They identified significant peaks in sediment concentration over time. They referred to sediment concentration peaks as sediment suspension events (defined as points where the sediment concentration is at least twice the background concentration). Smith and Mocke (2002) distinguish between the outer surf zone and the inner surf zone. For the outer surf zone they found the sediment suspension peaks to correlate with a series of breaking incident gravity waves. The percentages of suspension events preceded by 1, 2 or 3 breaking incident gravity waves are respectively 66%, 58% and 51%, while the average occurrence of breaking incident gravity waves was only 38%. This indicates that the breaking of waves play a significant role in the suspension of sediment.

Smith and Mocke (2002) indicate that events of increased high-frequency (1-10Hz) vertical oscillatory velocity to happen simultaneously or just after the occurrence of a series of bores. The same increased high-frequency oscillations events can be seen in the horizontal velocity record. Smith and Mocke (2002) interpreted these events as bore related turbulence. In Figure 2 a time series of sediment concentrations water surface elevations, orbital velocities and vertical velocities are shown. Breaking incident waves and the values of the calculated SIWEH function are also indicated. Large SIWEH values and velocity oscillations are indicative for turbulence. It can be clearly seen large SIWEH values occur just after or simultaneously with the passage of a series of bores. Smith and Mocke (2002) suggest that the high turbulence of breaking waves causes sediment suspension and thus peaks in SSC. There is however a lag between the increase of vertical velocity oscillations and sediment concentration peaks, this was also recognized by Yu et al., 1993. The lag increased when sediment concentrations are linked to velocity events higher above bed. This can be explained by the time needed to transfer orbital velocities in eddy-related turbulence from the water surface to the bed (yu et al., 1993; Smith and Mocke, 2002).
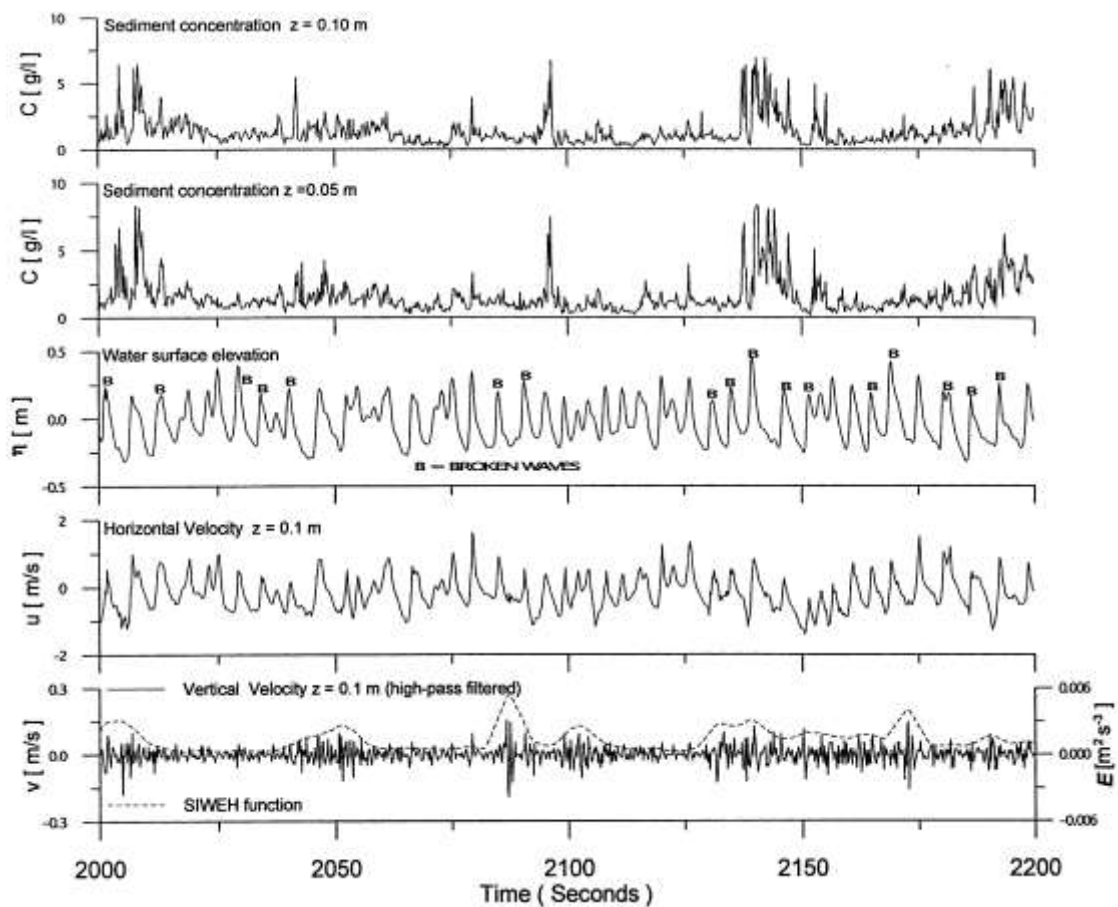
Figure 1,Time series of sediment concentrations at two highs above bed, colocated water surface elevations and colocated orbital and vertical velocities is shown. Capital B indicates breaking incident waves and the values of the calculated SIWEH function are indicated by the discrete line. (Smith and Mocke, 2002).

Already broken waves or bores, continuously create eddies at their front, can therefore still initiate sediment suspension long after the initial moment of breaking of the incident gravity waves (Yu et al. 1993). The magnitude of sediment suspended by bores can be significant compared to the suspension of sediment just after breaking of initial gravity waves (Yu et al., 1993; Smith and Mocke, 2002). For the inner surf zone when incident gravity waves are all transferred to bores, Smith and Mock (2002) could not identify a series of broken waves a source of energy for the sediment suspension. However correlation with of suspension events with large SIWEH values and increased velocity oscillations, indicative for increased turbulence, could again be made.

Although there is compelling evidence that gravity waves are responsible for the suspension of sediment, some authors report IG wave are also causing sediment suspension (Beach & Sternberg, 1988; Russel, 1993). Both authors suggest that IG waves are able to suspend sediment close to shore during storm conditions.

2.3 Mechanism of cross-shore suspended sediment transport mechanisms by Infragravity waves

2.3.1 Advection of sediment by IG waves from breaking point landward into the surf zone.

In the early 1990s the first field experiments considering the role of IG waves on SST were performed. (Aagaard & Greenwood , 1994) investigated the SST by IG waves on 4 locations on an inner bar within the surf zone of a dissipative beach. The directions and magnitude of the SST by IG was highly variable for the different locations and also variable during the storm on different locations. The highest SST by IG wave values were recorded on the crest of the inner bar. The derived the five most significant IG waves. Aagaard & Greenwood (1994) suggested that drift velocities associated with mostly standing waves transport sediment brought in suspension by gravity waves from nodal points to antinodes of the standing IG wave patterns. They did not directly analyze the SST associated with these drift velocities. But they concluded that the IG wave SST directions where always consistent with one or two of the identified significant standing wave patterns. This concept from Aagaard & Greenwood (1994) was also supported O'Hara & Huntley (1994), Houser & Greenwood (2005) among others.
More recently Aagaard & Greenwood (2008) measured sediment transport on two locations at the Danish beach of Skallingen and Staengehus and suggested that SST by IG wave occurs by means of advection away from high suspension maxima. Because most sediment is suspended by breaking incident gravity waves, they investigated the direction and magnitudes of net sediment transport as a function of the relative distance from the breaking point. Aagaard & Greenwood (2008) propose that sediment is mainly suspended by short breaking waves and IG wave oscillatory velocities transport the sediment away from the breaking point. Between the suspension maximum and a point landward of the suspension maximum a negative cross-shore gradient in the sediment concentration is present in the landward direction. This means that during the onshore phase of IG wave velocities, between these points, water with larger sediment concentrations is transported to a location landward with smaller sediment concentrations. During the offshore phase of IG wave velocities, between these points, water with smaller sediment concentrations is transported to a location more close to the suspension maximum with larger sediment concentrations. Therefore a net landward transport of sediment by IG wave exists landward of the suspension maximum.

Between a point seaward of the suspension maximum and the suspension maximum a positive cross-shore gradient in the sediment concentration is present in the landward direction. This means that during the onshore phase of IG wave velocities, between these points, water with smaller sediment concentrations is transported to a location closer to the suspension maximum with larger sediment concentrations. During the offshore phase of IG wave velocities, between these points, water with larger sediment concentrations is transported to a location further away from the suspension maximum with smaller sediment concentrations. Therefore a net seaward transport of sediment by IG wave exists seaward of the suspension maximum. The former explained transport mechanism results in the largest net sediment transport values close to the suspension maximum and smaller net sediment transport values with decreasing distance from the suspension maximum.

Figure 2 shows the IG wave STT fluxes against measurement position relative to the suspension maximum. The cross-shore IG wave STT flux is defined as the integral over the water column of the cross-shore velocity and the sediment concentration. Both the cross-shore velocity and the concentration profile over depth are hard to estimate with a limited number of sensors. The authors considered the SSC and the velocity measured by the lowermost exposed sensor (nominally located 5cm above the bed) to be a reasonable estimate of the local SST characteristics. The cross-shore IG wave STT flux was therefore calculated assuming one value for SSC and one velocity for the whole water column, the values measured by the lowermost exposed sensor. The suspension maximum was not based on directly measured sediment concentrations but peaks in the relative wave height (ratio between local wave height and water depth) were considered surrogates for the position of suspension maxima. In Figure 2A all the cross-shore IG wave STT fluxes from four field experiments is shown with distance from the suspension maxima.
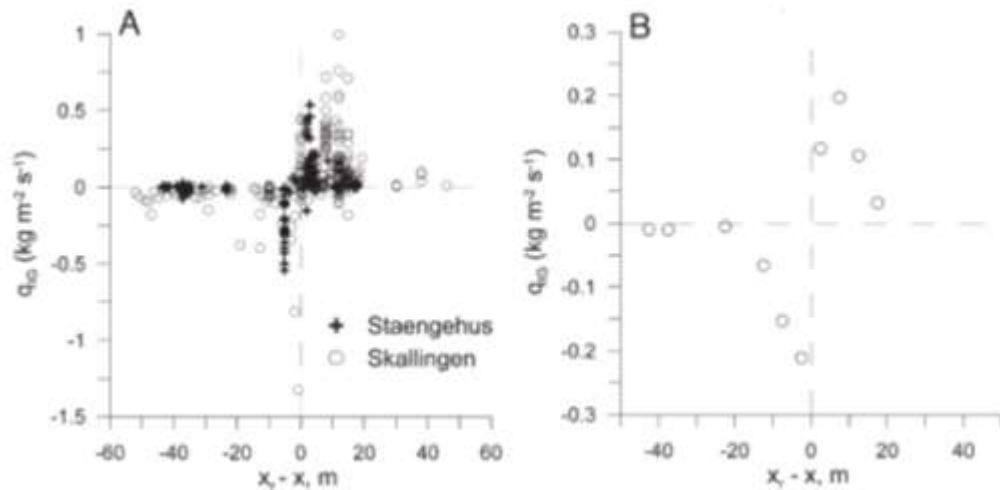
Figure 2 A) IG wave SST fluxes plotted against measurement position relative to the suspension maxima. Positive sediment fluxes signify a net onshore sediment transport and positive values of indicate that the measurement position was located landward of the suspension maximum. B) graph with the computed cross-shore IG transport shape function from the data in A. The measurements have been aggregated into 5 m cross-shore bins. (After Aagaard & Greenwood, 2008)

From the cross-shore IG wave STT flux data it can be clearly seen that the cross-shore IG wave STT fluxes are predominantly directed offshore seaward of the suspension maxima (81% of the cases) and onshore landward of the suspension maxima (85% of the cases). To reduce the scatter and highlight the relationship between cross-shore distance from the suspension maxima and the cross-shore IG wave STT flux Aagaard & Greenwood (2008) computed the average cross-shore IG wave STT flux for 5 meter cross-shore bins. They refer to the graph of the mean cross-shore IG wave STT per bin as the IG transport shape function. Figure 2 B shows the graph of the IG transport shape function. The occurrence of predominantly onshore transport shoreward of the breaking point is also found by Beach & Sternberg (1996), Osborne & Greenwood (1992a) and Osborne & Greenwood (1992b). The theory of Aagaard & Greenwood (2008) also fit with the data Aagaard & Greenwood (1994) collected. The measuring station on the seaward slope of an outer sand bar, located in shoaling zone IG SST was offshore directed. The measuring station on the crest of a sand bar and landward of the sand bar, both in the surf zone, showed positive IG wave SST values. On the crest of the sand bar most of the gravity waves where breaking and the SSC values measured where the highest. The most landward station on the slope of a small inner bar, located in the inner surf zone, however showed negative IG wave SST. This is therefore not explained by the advection mechanism of Aagaard & Greenwood (2008).

2.3.2 Negative modulation of gravity waves by infragravity waves.

The investigations by Alsina & Cáceres (2011), Smith & Mocke (2002) and Voulgaris & Collins (2000) suggest that the interaction between gravity waves and long waves results in offshore SST by IG waves the surf zone. Although processes associated with a series of breaking and broken incident gravity waves suspend sediment, peaks in the sediment concentrations occur on a IG time scale (Smith & Mocke, 2002). Alsina & Cáceres (2011) as well as Smith & Mocke (2002) identified the series of bores and therefore peaks in sediment concentration to coincide with the peaks in offshore directed long-wave induced horizontal velocities. Because the peaks in sediment concentration are present during off-shore directed part of the oscillatory motion, transport on a IG time scale is offshore directed.

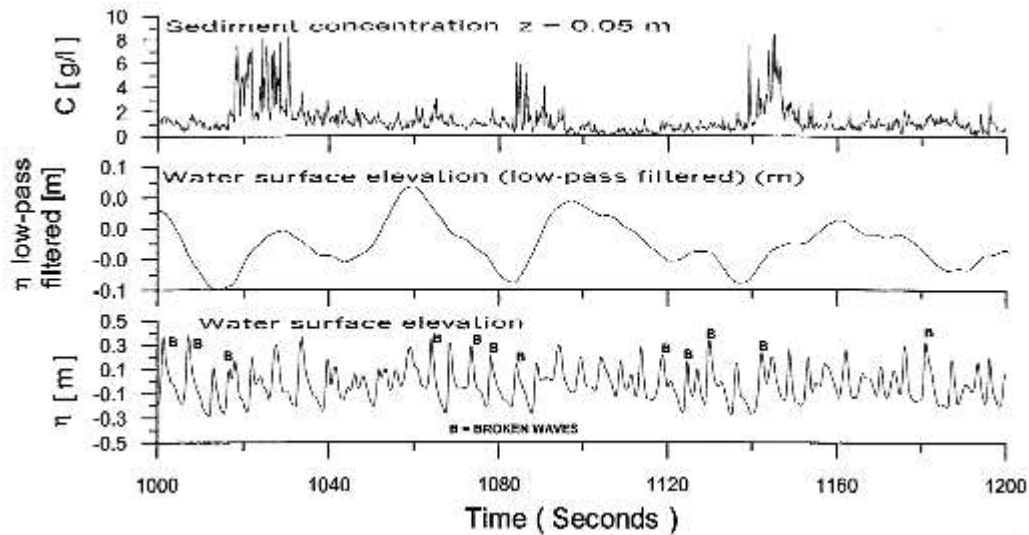Smith & Mocke (2002) showed that peaks in SSC occur regularly on an IG time scale. In Figure 3 Time series of sediment concentration, low-pass-filtered (at cut-off frequency of 0.05 Hz) water surface elevation and the water surface elevation with indicated breaking waves. Figure 3 Smith & Mocke (2002) plotted a time series of sediment concentration, low-pass-filtered (at cut-off frequency of 0.05 Hz) water surface elevation and the water surface elevation with indicated breaking waves. Three events of large SSC (on 1025,1085 and 1045 seconds) can be identified with a period of about 60 seconds. Cross-correlation of peaks in SSC and IG wave troughs water indicates a significant relationship. Series of incident waves are clearly breaking at the lowest IG wave troughs, inducing sediment suspension just after breaking. Smith & Mocke (2002) propose the limited water depth is likely to (1) ensures the breaking of already very asymmetrical gravity waves inducing associated turbulence and sediment suspension and (2) limited water depth causes eddies to propagate more easily towards the bed and create more turbulence and thereby sediment suspension. However they also propose the successive stirring by the breaking of a series of large waves in a wave group to be an explanation for the large sediment suspension peaks, meaning that the limited water depth is not driving factor but only occurs on the same time scale as the successive breaking of the largest waves in the wave group. The times series measured by Smith & Mocke (2002) on a sheltered very low energy beach where the relation between IG wave troughs and large peaks in sediment concentrations was not found. The less strong relationship between suspension events and bore related turbulence is probably caused by the fact that not all high velocity events create enough turbulent energy to cause a significant peak in sediment concentrations.

Figure 3 Time series of sediment concentration, low-pass-filtered (at cut-off frequency of 0.05 Hz) water surface elevation and the water surface elevation with indicated breaking waves (Smith & Mocke, 2002).

Alsina & Cáceres (2011) used a flume experiment to evaluate the suspended sediment concentrations in the inner surf zone. Suspended sediment concentrations peaks did not seem to correlate well with the incident bore height or short wave scale horizontal velocity, meaning that neither the highest bores nor associated large negative or positive velocities coincided with the highest sediment concentrations. The highest suspended sediment concentrations were observed to occur by combined action of incident bores and the trough of long-period water level oscillations. They also concluded very low water levels under the trough of the IG waves apparently promote sand stirring by gravity wave bores resulting in offshore IG wave SST. Voulgaris & Collins (2000) also indicated the limited water depth associated with the passing of IG wave trough causes incident short frequency bores to create more turbulence and thereby increased sediment suspension (i and v in Figure 4).
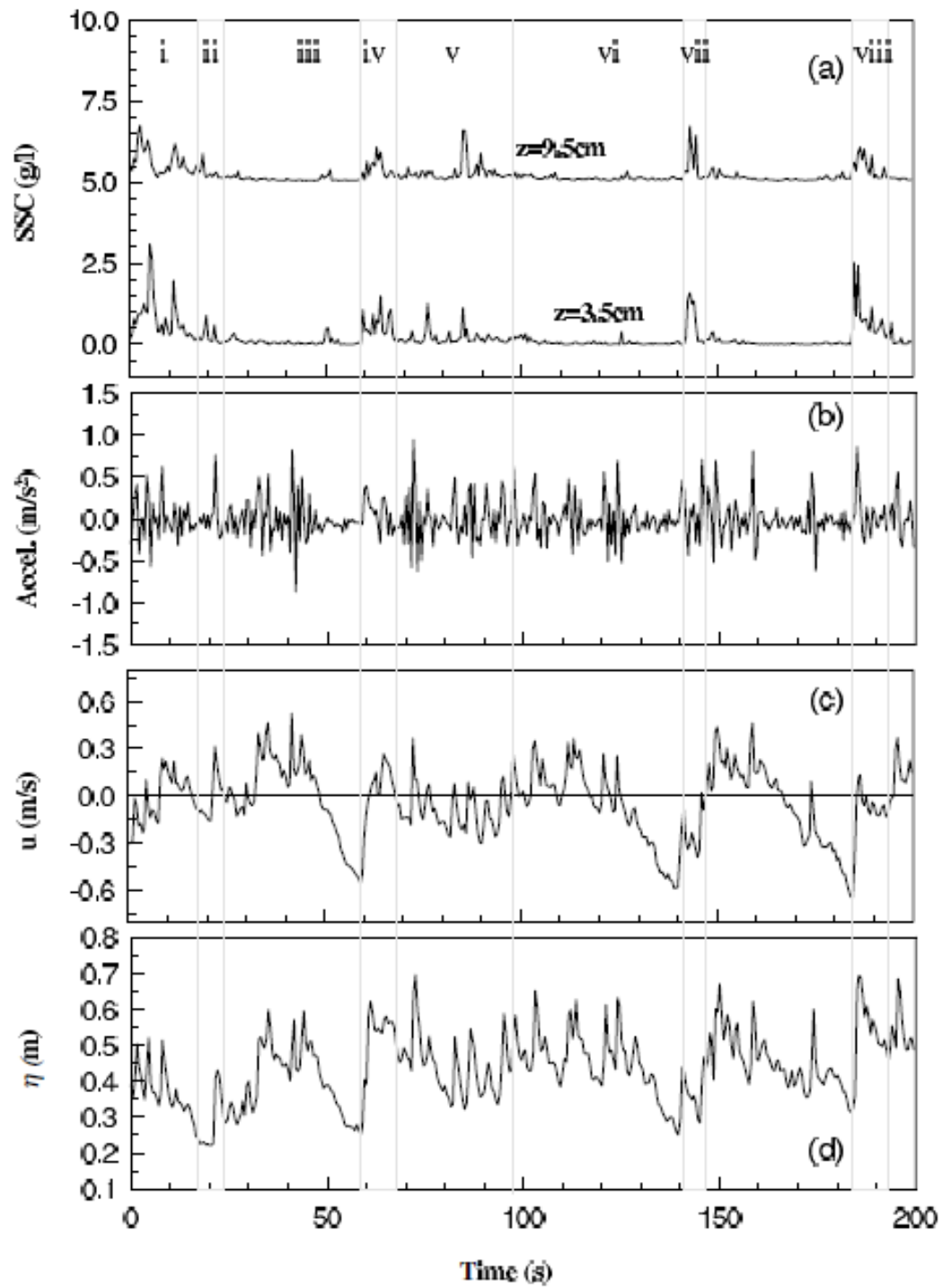
Figure 4 Time series of sediment concentration, acceleration, vertical velocity and water surface elevation (Voulgaris & Collins, 2000).

2.3.3 Positive modulation of gravity waves by infragravity waves.

Houser & Greenwood (2007) propose mechanism by which IG waves promote positive SST. Houser & greenwood (2007) concluded that interaction between gravity and IG waves cause gravity bores to suspend more sediment on the onshore phase of the IG oscillatory velocity phase. Gravity bore seem to have a higher amplitude and asymmetry during onshore IG wave velocities compared to offshore IG wave velocities. Because more sediment is suspended during offshore IG wave, advection by IG waves result in net positive SST.

Houser & Greenwood (2007) measured the velocity and pressure at three stations located around a swash bar at the beach of Skallingen, Denmark. At station one they measured SSC and they monitored the morphology of the swash bar during one tidal period. Figure 5 shows the morphology measurements and the location of the stations. In the same figure total SST as well as the SST for the oscillatory and mean components are depicted. It can be clearly seen that the IG wave SST dominates the whole tidal period except for the beginning of the tidal period. Although the SST was IG frequency dominated peaks in SSC occurred on a gravity wave scale. Furthermore the peaks in SSC were restricted to the onshore phase of the IG oscillatory velocity for most of the period, except for the beginning of the tidal period were peaks in SSC occurred on both the onshore and the offshore phase of the IG oscillatory velocity.
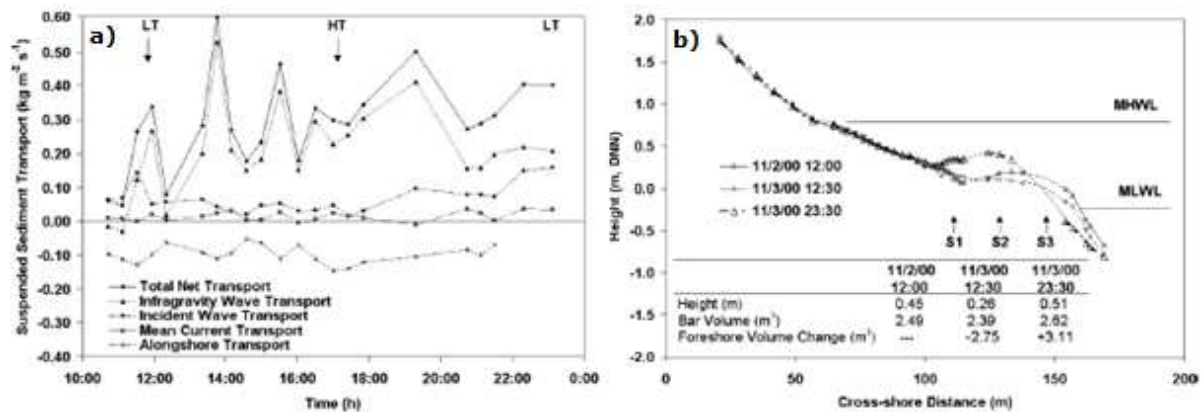
Figure 5 a) total, oscillatory and mean components of SST during the second tidal period 11/3 10.00hr till 11/3 23.30hr. b) morphology measured on three moments in time, the second and the third measurement show the morphological change during the tidal period where SST was measured (Figure 5a). S1, S2 and S3 indicate the locations of measurement station 1,2 and 3 respectively (Houser & Greenwood, 2007).

By further inspection of the velocity record Houser & Greenwood (2007) revealed that the average wave height as well as the asymmetry of gravity waves proved to be larger on the

onshore phase of the IG velocity oscillations. The difference between the onshore and offshore phase (Δon/off) increased with decreasing water depth for the average wave height. Figure 6a) shows the relation between Δon/off IG oscillatory velocity as a function of water depth as well as the Δon/off IG oscillatory velocity over the whole tidal period (Figure 6 b). Note that during low tide and small water depth, Δon/off oscillatory velocity is also smaller. On the contrary Δon/off asymmetry of gravity waves increased with increasing water depth (Figure 6 d). The asymmetry of gravity waves for the complete velocity record seemed to dramatically increase for station one at the end of the tidal period, resulting in an increasing gradient in asymmetry of gravity waves over time (Figure 6 c).
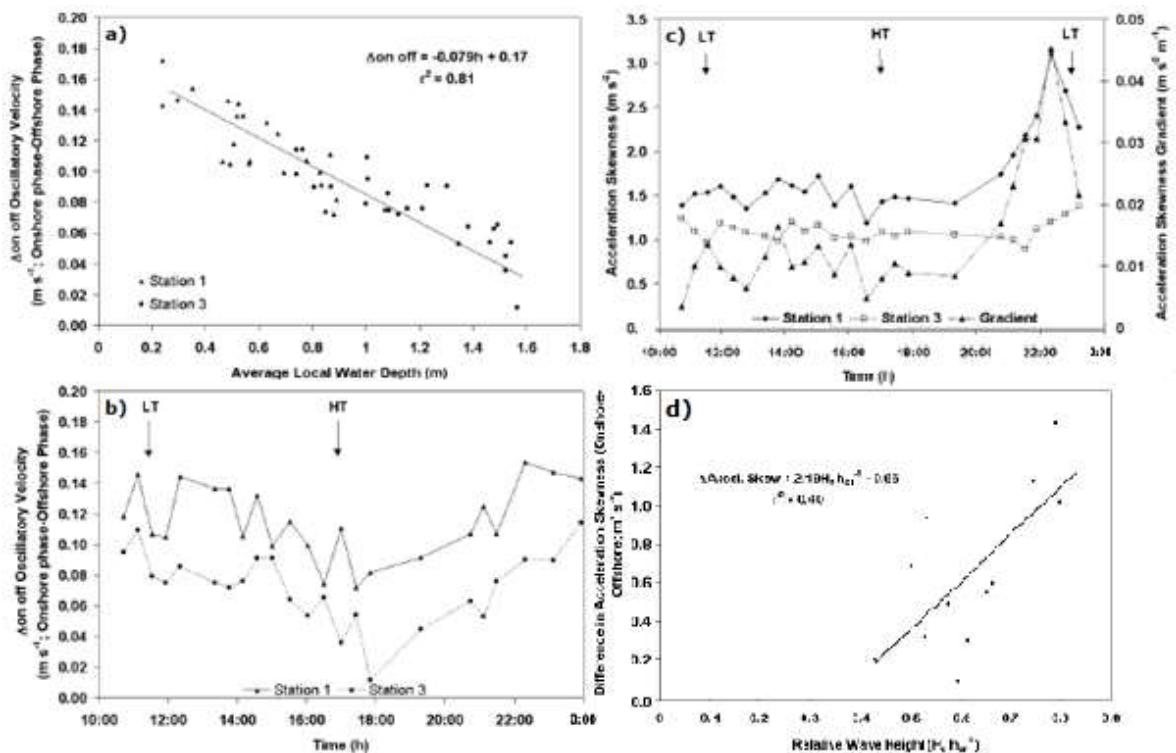
Figure 6 a) The relation between Δon/off IG oscillatory velocity as a function of water depth. b) Δon/off IG oscillatory velocity over the whole tidal period. c) asymmetry of gravity waves for the complete velocity record during the whole tidal period. d) Δon/off asymmetry of gravity waves as a function relative wave height (Houser & Greenwood, 2007).

Comparing the peaks in SSC with the velocity record showed the asymmetrical leading face of gravity bores just preceded or coincided with the peaks in SSC, suggesting an relation between

gravity wave asymmetry and sediment suspension. Wave asymmetry doesn't initiate differences between sediment suspension by velocity maxima or minima based on the velocity record. Nielsen (1992) cit. Butt & Russell (1999) showed a mechanism by which sawtooth-shaped waves are able to create significant peaks in sediment suspension at the passage of the steep-fronted part of the wave. They explain this in terms of boundary layer growth times. During the passage of the steep-fronted wave form acceleration is large, therefore the boundary layer has less time to develop. Free stream velocities penetrates closer to the bed, therefore causing higher bed-shear stresses and associated sediment suspension. The fact that gravity wave asymmetry seems to be larger during onshore IG wave velocities results in positive IG wave SST.

2.3.4 Sediment suspension by infragravity waves

Beach & Sternberg (1988) were one of the first to perform a field experiment involving measurements of SSC by OBS-instruments on different highs above the bed. They analyzed time series from a period where the oscillatory velocity record was dominated by IG waves. They concluded that during the offshore IG orbital velocity phase, shear stress at the bed creates enough turbulence to suspend sediment. They recognized that the largest suspension event, about 3-4 higher SSC than suspension events by gravity waves, occurred around just before the highest offshore IG wave velocities. The large SSC during the offshore IG orbital velocity phase let to mostly negative IG wave SST values. Some of these suspension events where followed by even higher SSC values after flow reversal to positive IG velocities. SSC remained high during the onshore IG velocity phase leading to onshore total SST by the IG wave. Figure 7 shows the time series and SSC profiles for one of the IG waves causing large sediment suspension during the offshore IG velocity phase.
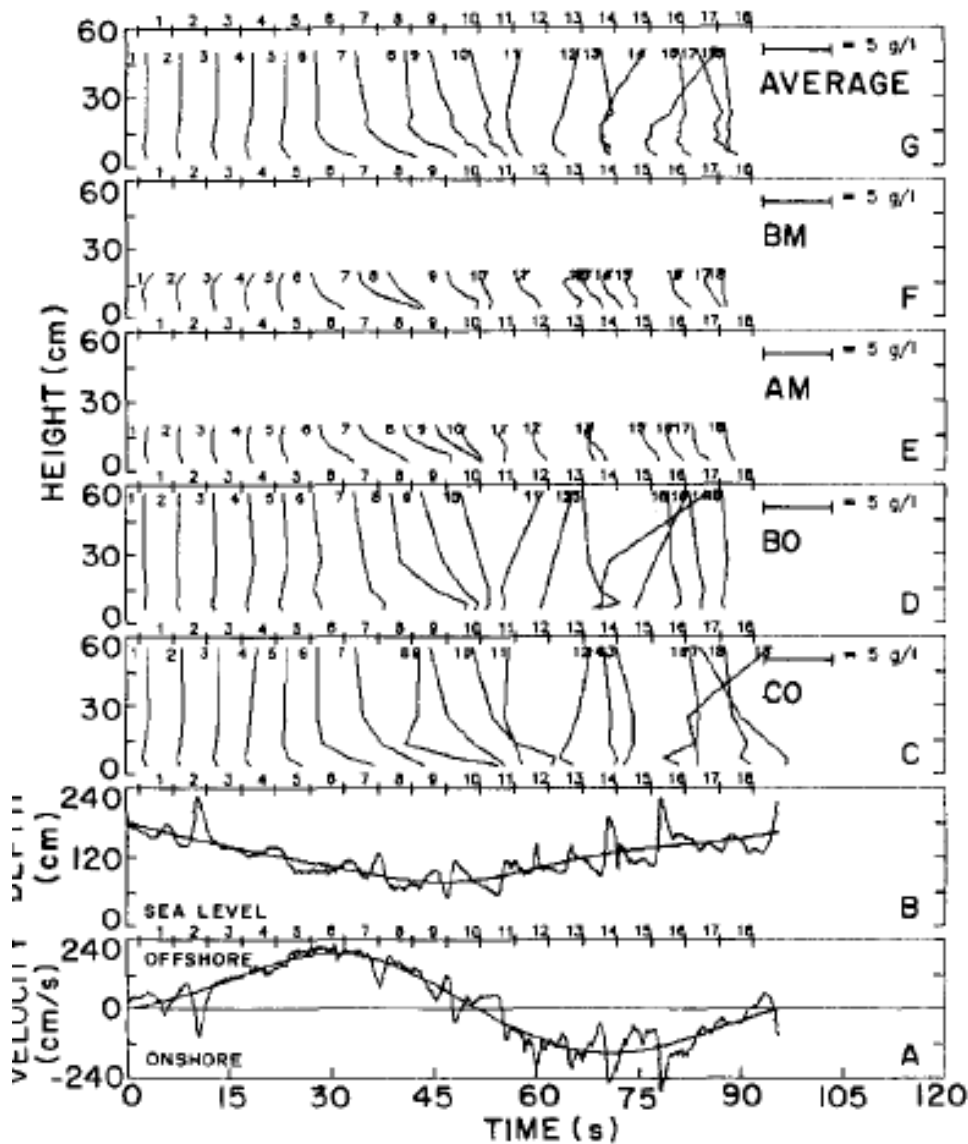
Figure 7 time series of the cross-shore velocity (A) and sea level fluctuation (B) for one particular IG wave causing larger SSC values. C-F indicate the vertical distribution of SSC for four different measuring stations based on a number of OBS devices placed in the vertical for every station. Vertical SSC profiles are averaged over 5 sec resulting in 18 profiles for the total. G gives the average profiles of the four different measuring stations for 18 profiles (Beach & Sternberg, 1988).

They measured SSC and cross-shore velocity at four measuring stations in the surf zone. Every measuring station was equipped with multiple OBS sensors in the vertical. They analyzed the time series the vertical SSC profiles, cross-shore velocity and sea level fluctuations for every IG wave separately. For every IG waves the SSC profiles where averaged over 5 seconds. For profile 1 in Figure 7G vertical distribution of sediment is uniform and SSC is low. The next 15-20 seconds (profile 1-4) offshore IG velocity increased but does not affect the vertical distribution of sediment. Subsequently a vertical gradient develops for profile 5-10, meaning the SSC at the bed is larger than higher at the water column.

The maximum vertical gradient develops for profile 7 when the offshore orbital velocity peaks, profile 8-10 show a smaller vertical gradient and increasing total SSC. For profile 11-15 the SSC increased dramatically just after flow reversal. Also the vertical gradients inverted, the SSC being larger, higher in the water column. Large SSC then persisted till the peak in onshore directed IG wave velocities. For this wave the total SST was directed onshore. Because both the development and decay of the SSC profile gradients occurred on a IG time scale Beach & Sternberg (1988) assume that IG wave orbital velocity induced shear stress at the bed is enough to create turbulence and suspend sediment. To test their assumption, they constructed a one-dimensional time-dependent turbulent diffusion model. The model predicted the shear stress and associated SST profiles reasonably well. The model could not predict the occasional large SSC values during flow reversals and the inversion of the SSC profile. This is important because it emphasizes the fact that the large SSC values during flow reversal are not due to turbulence induced by IG wave oscillatory velocity induced shear stress , but should be caused by another mechanism.

Russell (1993) also suggest sediment suspension events to coincide with the strongest near-bed velocities during the offshore phase of IG wave velocity oscillation. Under low energetic conditions (Hsig =0.4m). Russell (1993) observed that the mean transport component was dominant and gravity waves dominated the oscillatory velocity record. The author did not identify a mechanism by which IG scale transport was generated under these conditions. However during storm conditions (Hsig ≈3.0m), especially during the ebbing tide on the storm day, IG scale sediment transport contributed 66% to the total sediment transport while the mean component only accounted for 31% of the total transport (Russell, 1993). During the storm day cross-shore velocity oscillations by IG waves dominated the surf zone. Figure 8 shows the time series of wave amplitude, cross-shore velocity, alongshore velocity, SSC and SST. In Figure 8 it can be visually confirmed that sediment transport events coincided with the strongest near-bed velocities during the offshore phase of IG wave velocity oscillations, leading to negative IG wave SST. The occurrence, magnitude and duration of the suspension events increased with decreasing water depth during storms and suspension was more likely to occur when the offshore IG wave velocity oscillations coincided with offshore mean velocities (ebb tide in combination with offshore directed undertow velocities). Apparently IG waves are able to suspend more sediment when the undertow velocities and the IG oscillatory velocities are acting in the same direction. This could be explained by the fact that codirected oscillatory and mean velocities create a larger bed-shear stress that opposed IG oscillatory and mean velocities.
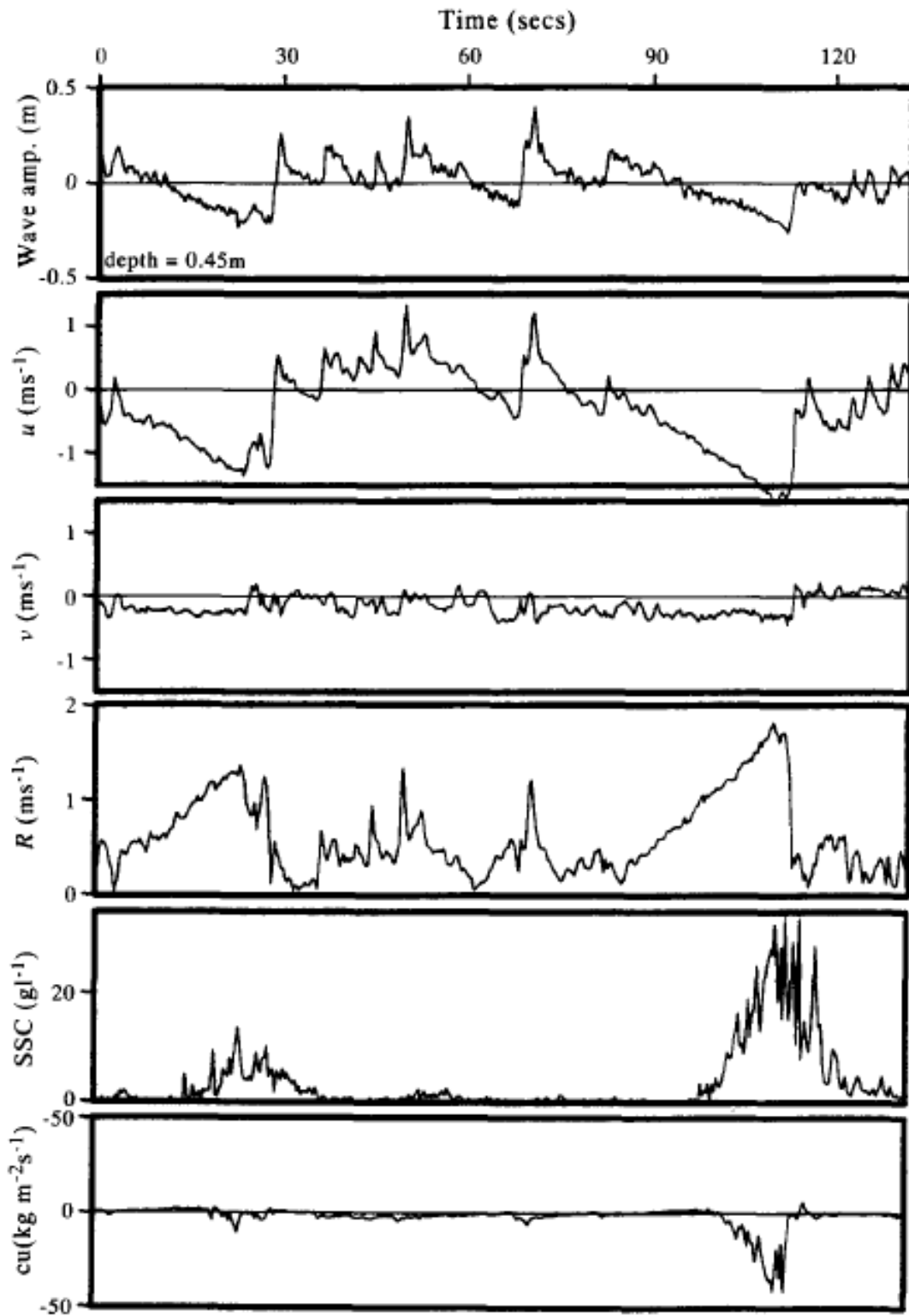
Figure 8 Simultaneous time-series of waves amplitude, cross-shore velocity (u), alongshore velocity (v), Resultant velocity (R, magnitude of the resultant cross-shore velocity vector and alongshore velocity vector), suspended sediment concentration (SSC) and the suspended sediment transport (cu) during storm night in the inner surf zone from the investigation of Russell (1993).

2.3.5 Negative-positive flow reversals, bore turbulence and bore collapsing on a IG time scale.

Many authors showed that bore collapsing, bore turbulence and interaction between negative and positive flow just after negative-positive flow reversals on IG scale cause large SSC events contributing significantly to positive SST by IG waves in the inner surf zone (Butt & Russell, 1999; Voulgaris & Collins, 2000; Butt et al. 2004; Butt & Russell, 2005; Masselink et al., 2005; Aagaard & Hughes, 2008; Butt et al., 2009). Most of the authors focus on the swash zone, cross-shore velocity in the swash zone of a dissipative is often characterized by large negative asymmetry and rapid negative-positive flow reversals. But rapid negative-positive flow reversals are proven to be also important in the inner surf zone (Voulgaris & Collins, 2000; Butt et al. 2004; Butt & Russell, 2005; Masselink et al., 2005; Butt et al., 2009). Some of the articles discussed in this section focus therefore on the swash zone, but are relevant for the inner surf zone as well.

Butt & Russell (1999) measured sediment concentrations in the swash zone of a dissipative beach under calm and storm conditions. Figure 9 shows the records of the most seaward end of the swash zone for calm conditions (A) and storm conditions (B). Analysis showed IG wave asymmetry and skewness are often large (Butt & Russell, 1999). Especially under storm conditions the skewness was significantly negative (Butt & Russell, 1999). Looking at the records it is clear that peaks in sediment suspension occur on IG time scale under both calm and storm conditions. The peaks in SCC seem to occur just after the peak in offshore velocity during flow reversal. Butt & Russell (1999) correlated gradients in velocity record with the sediment suspension events (Figure 9A) and conclude that large positive peaks in acceleration prior to the peaks in SCC are the sediment suspension. Butt & Russell (1999) also drew an arbitrary threshold line indicating the rapid velocity change must be of a certain magnitude to generate sediment suspension. Under storm conditions peaks in the sediment concentration coincide with large positive peaks in acceleration as well as the passage of large IG wave troughs at 45 and 170 sec in in the storm record, Figure 9B (Butt & Russell, 1999).
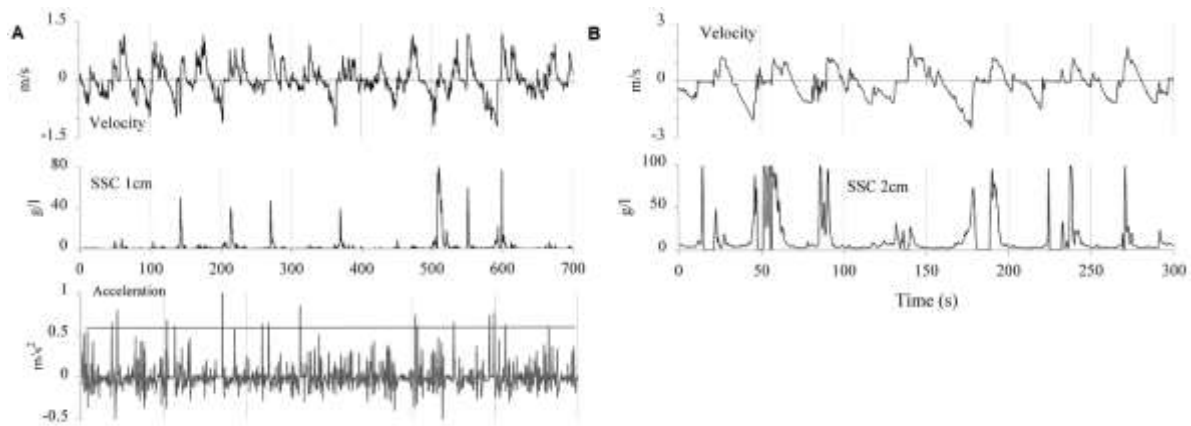
Figure 9 time series of vertical velocity, sediment concentration and acceleration for calm conditions (A) and storm conditions (B) at the most seaward end of the swash zone (after Butt & Russell, 1999).

Nielsen (1992) cit. Butt & Russell (1999) showed a mechanism by which sawtooth-shaped waves are able to create significant peaks in sediment suspension at the passage of the steep-fronted part of the wave. They explain this in terms of boundary layer growth times. During the passage of the steep-fronted wave form acceleration is large, therefore the boundary layer has less time to develop. Free stream velocities are evident closer to the bed, therefore causing higher bed-shear stresses and associated sediment suspension. Butt & Russell (1999) did no measurements to confirm this theory.

Voulgaris & Collins (2000) found that in the inner surf zone, gravity wave bores (ii, iv, vii and viii in Figure 4) were able to generate large SCC events just after the flow negative-positive flow reversal. The strong offshore currents were backwash events on a IG scale capable of making bores collapse just after the flow reversal (peak in total offshore velocities). Note the water depth is close to zero, meaning the influence of backwash on bore collapsing is probably relevant on the transition between the surf zone and the swash zone only. The bore collapse generated enough turbulence to generated peaks in the sediment concentration. Butt et al. (2004) confirmed that large SSC events after negative-positive flow reversal were indeed caused by bore turbulence. Butt et al. (2004) used the earlier explained TKE values as an indicator of turbulence and investigated if bore related turbulence was an important factor in sediment suspension on the surf/swash zone transition. Figure 10 shows a representative section of the times series used by Butt et al. (2004). Some of the large peaks in SSC clearly coincide with TKE speaks and both occur during the sharp transition from offshore to onshore velocities. Vertical broken lines in Figure 10 indicate the onset of the sediment suspension events and show that TKE values are already large while near bed velocities are still directed offshore. The TKE events start when the bore arrives and backwash still dominates the lower water column, but reaches his maximum during the passage of the bore forcing the velocities onshore (Butt et al., 2004).
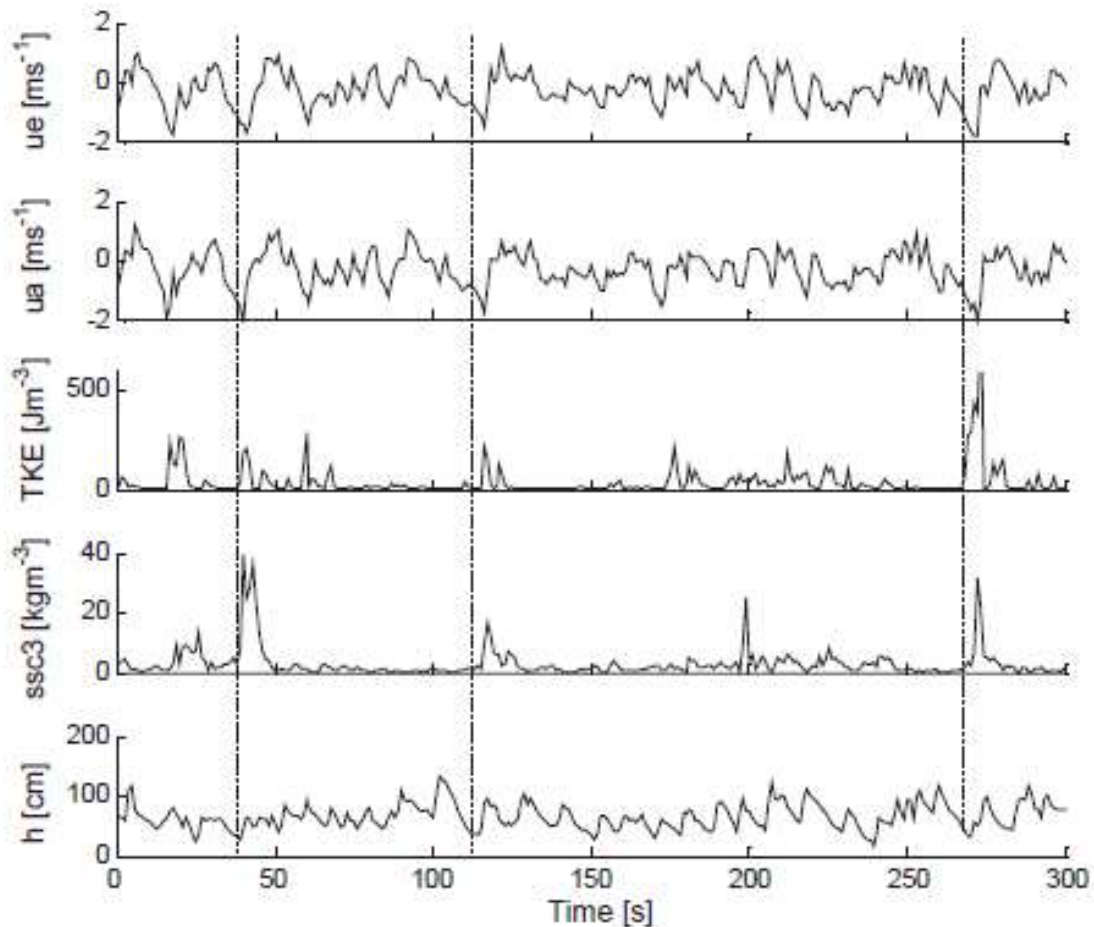
Figure 10 representative section of the time series used by Butt et al. (2004) for TKE analysis. Cross-shore velocity was measured at z= 3cm by an EMCM (ue) and at z= 7.5 cm by an ADV (ua). TKE was calculated using the ADV data at z= 7.5cm. Sediment concentration (ssc3) was measured at z= 3cm and the last graph shows the water depth. Positive values of velocity are onshore directed and the vertical broken lines indicate the beginning og significant TKE end SSC events (Butt et al., 2004).

Because the TKE values are higher during the passing of the bore than at the end of the backwash indicates bore turbulence to be the dominant suspension mechanism. If near bed velocity bed shear stress would have been the dominant mechanism TKE values are the highest during shallow high velocity flow i.e. the end of the backwash. Butt et al. (2004) did not calculate any transport values however the SSC were already up when in at least a part of the water column the velocities were still directed offshore, after flow reversal velocities are fully positive, leading to partly positive and negative transports (Butt & Russell, 2005; Masselink et al., 2005; Butt et al., 2009).

Butt & Russell (2005) argue that especially during high energy conditions bores are counteracted by backwash events leading to a stationary hydraulic jump and sometimes even to bore collapses. If this turbulence reaches the bed it can suspend sediment. This idea is confirmed by Longo et al. (2002), Butt et al. (2004), Masselink et al. (2005) and Butt et al. (2009). The swash-zone hydraulic jumps are more prevalent during high energy conditions when high-velocity backwashes predominate. For this reason, Butt & Russell (2005) suggest the offshore sediment transport associated with advection of sediment suspended by hydraulic jumps in fact contributes to the offshore directed sediment transport measured by Butt & Russell (1999) which they associate with negative velocity skewness. Note that both the investigations of Butt & Russell (1999) and Butt & Russell (2005) were performed in the swash zone, but could be relevant for the inner surf zone.

Masselink et al. (2005) investigated sediment transport in the swash and surf zone of a dissipative beach. The swash zone is typically defined as the part of the beach submerged less than 100% of the time and the surf zone as being always submerged. They defined a transition zone as the zone with an inundation percentage of 90 to 100% and showed that this zone was characterized by the largest SST fluxes. Figure 11 shows the water depth, cross-shore velocities and the SST flux measured by Masselink et al. (2005). In this transition zone Masselink et al. (2005) identified large SST fluxes to be related to IG scale flow reversals. Masselink et al. (2005) also suggest the initiating of SST to be mainly caused by bore turbulence because the onshore suspended sediment flux depends more on water depth in front of the bore rather that the flow velocity in the bore. Confirming sediment transport associated with bore turbulence rather than wall (turbulence created by bed-friction and flow) turbulence.
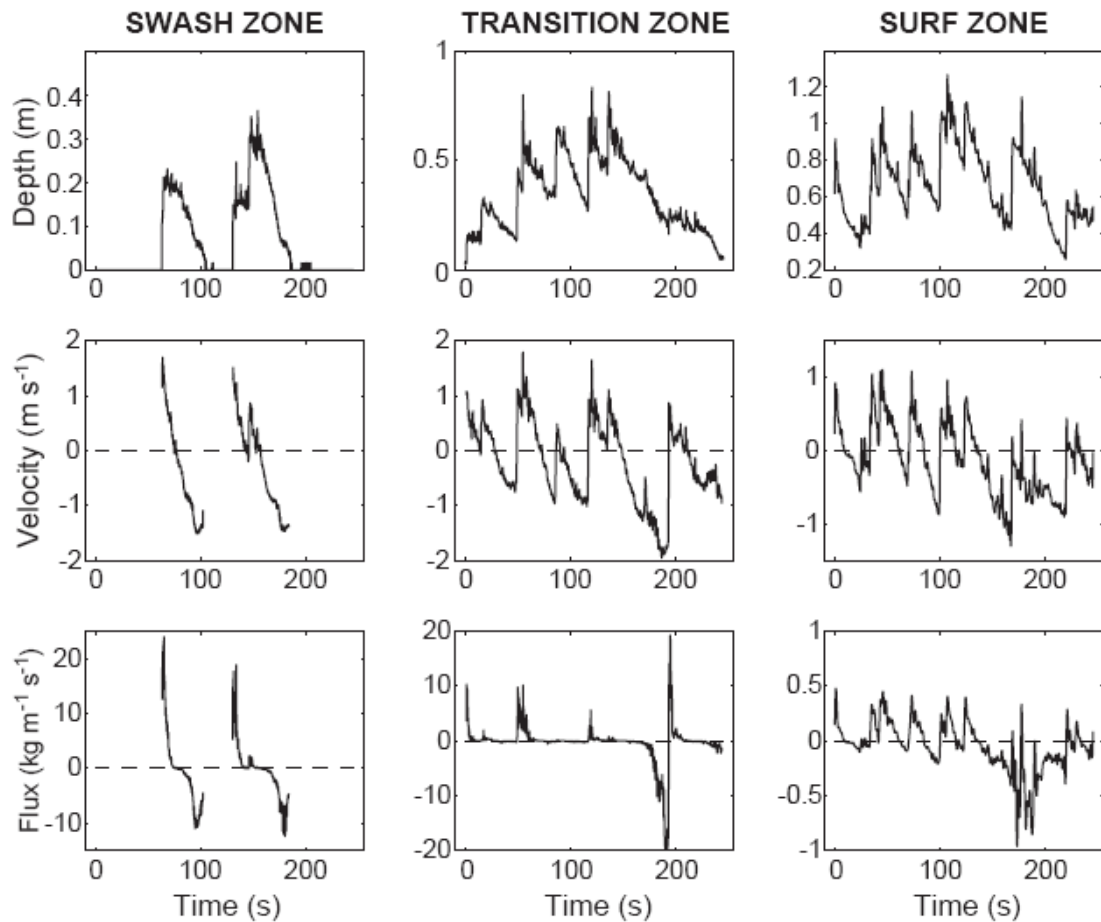
Figure 11 time series of water depth, cross-shore velocities (0.03m above bed) and the suspended sediment flux (integrated over the water column) in the swash, transition and surf zone measured by Masselink et al. (2005) during storm conditions and high tide (Masselink et al., 2005).

Butt et al. (2009) examined events of large sediment fluxes on the transition between the swash and surf zone. Figure 12 shows the sediment fluxes, suspended sediment concentrations and the velocity values 3 cm above the bed. Note that the suspended sediment fluxes during the sediment suspension events are partly positive and negative just like Butt & Russell (2005) and Masselink et al. (2005) already showed. Butt et al. (2009) examined the velocity in the whole water column for these IG scale SST events in details. They summed the velocity and velocity shear values for multiple of these SST events and plotted the values over water depth and time. They concluded that at the asymmetrical flow reversal the velocity at the bottom was often still offshore directed while the velocity higher in the water column are already directed onshore. This causes velocity shear stress in the mid-water column rather that near bed-velocity bed shear stress. Butt et al. (2009) suggest that the interaction between the onshore directed velocities and the offshore velocities create the bed shear stress creating sediment suspension.
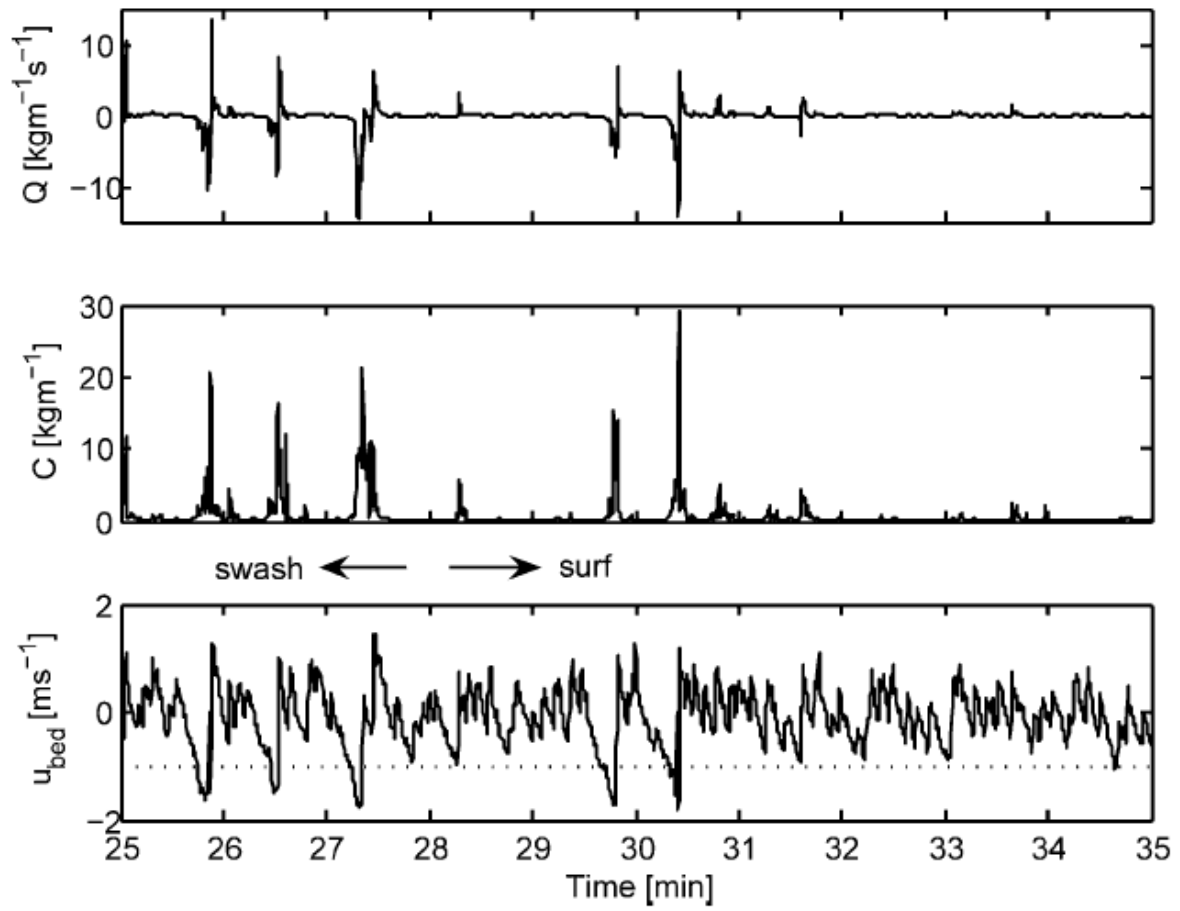
Figure 12 time series of suspended sediment transport, suspended sediment concentrations cross-shore velocities (0.03m above bed) on the surf/swash transition zone (Butt et al., 2009)

2.3.6 Literature summery, unifying transport theory and research questions.

It is clear that no consensus between different investigations about the dominant sediment mechanism is reached yet. Without knowing the transport mechanism it is impossible to explain the inconsistency in transport magnitude and direction due to IG waves found by different investigations. In literature the following five IG wave SST mechanism are suggested by different authors:

1. Positive suspended sediment transport by infragravity waves because sediment suspended by breaking gravity waves is advected from breaking point landward into the surf zone.
2. Negative suspended sediment transport by infragravity waves because sediment is mainly suspended by gravity waves during the negative infragravity velocity phase.
3. Positive suspended sediment transport by infragravity waves because sediment is mainly suspended by gravity waves during the positive infragravity velocity phase.
4. Negative suspended sediment transport by IG waves due to sediment suspension by infragravity waves
5. Positive suspended sediment transport by IG waves due negative-positive flow reversals bore turbulence and bore collapsing on a IG time scale.

Although many authors focus on one mechanism only, the mechanism are not mutually exclusive. Mechanisms 1-5 all influence the SST in a different way. According to mechanism 1 the IG waves only transport sediment suspended by gravity bores. Mechanism 2 and 3 IG waves affect also the suspension by gravity waves restricting sediment suspension to either the offshore or onshore IG velocity phase. This way the IG wave modulate the gravity wave height and directly influence suspension by gravity waves. The IG waves have to be important with respect to gravity waves in the velocity and wave spectra to be able to modulate the gravity waves. For mechanism 4, the IG waves start to dominate in the total oscillatory velocity record even causing sediment suspension by IG orbital velocity directly. According to mechanism 5 the gravity bores are affected in such a way that they cannot propagate during the offshore IG velocity phase, because it is fully dominated by negative velocities. After the negative-positive flow reversal the inaction between positive and negative flow plus the accumulated bore energy can now cause sediment suspension. For mechanism 4 and 5 it seems that the velocity and wave spectrum needs to be dominated by the IG frequency.

Relative importance of IG waves in the total velocity and wave spectrum seems therefore important explaining the different SST mechanisms.

One or more mechanisms could be active in the surf zone under different conditions. Studying the conditions under which the mechanisms are identified by the various authors, three parameters are considered to be important for the determination of the different IG wave SST mechanisms and the explanation of the IG SST pattern:

1. The cross-shore location within the surf zone: this parameter is relevant for mechanism 1-5 and is considered to be the most important factor (therefore indicated in bold). Mechanism 1 was relevant in the outer surf zone. Aagaard & Hughes (2008) already used the cross-shore distance from breaking point as a parameter and explained that the SST magnitude reduces with distance from the breaking point of waves, due to transport by means of advection. Mechanism 2 is suggested to occur in both the inner and outer surf zone. Mechanism 3 is suggested for the inner surf zone only. Mechanism 4 and 5 are observed to happen only in the inner surf zone close to the swash zone.

2. The mean water depth: a parameter mentioned to be of importance for mechanism 2, 4 and 5. For IG waves to effectively modulate the water depth the amplitude of the IG waves should be significant compared to the water depth (Alsina & Cáceres, 2011). The SST related to the suspension by IG waves requires also very limited water depth and is therefore restricted close to the shoreline (Russell, 1993). Also mechanism 5 only occurs close to the swash zone at low mean water depths (Butt & Russell, 2005)

3. Offshore wave height is an important variable for both mechanism 4 and 5. Both mechanisms are reported to dominate during storm conditions (Russell, 1993; Butt & Russell, 2005).

Besides the lack of consensus on the means by which IG wave cause SST and the overall direction of the IG wave SST, there are other limitations to the current state of knowledge. A limited amount of measurements especially field measurements under different conditions focuse on IG wave SST. Different transport mechanisms are mostly determined by visual identification of small data series. This research subject needs a research containing a high amount of measurements, to identify the importance of the mechanisms, relate them to the different variables above and create a unifying theory of SST by IG waves in the surf zone of a dissipative beach.

In order to determine the role of IG waves in the total cross-shore sediment transport in the surf zone of a dissipative beach, three research questions were formulated:

1. How did the relative importance of infragravity compare to gravity waves relate to cross-shore location within the surf zone, offshore wave height and water depth?

2. How did the suspended sediment transport by infragravity waves relate to the cross-shore location in the surf zone?

3. Which mechanisms were most likely responsible for the infragravity wave suspended transport pattern in the surf zone?

3 Research Methods

3.1 Field site and data collection

A 5-week field experiment was conducted at the beach of Egmond aan Zee, The Netherlands (Figure 13), from September 27th till November 1st, 2011. The beach of Egmond aan Zee has an approximate has north-south orientation, with a 7° deviation in the northeast-southwest direction. The beach of Egmond aan Zee is located at the eastern border of the North Sea, a shallow semi-enclosed marginal sea of the Atlantic Ocean. The intertidal zone at the beach of Egmond aan Zee generally has a cross-shore width of 50-100m, typical beach slope of ~1:30 and includes quasi-rhythmic intertidal bars intersected by rip channels. The average significant wave height per year at a water depth of about 25 m is approximately 1.2 m with a wave period of about 5 s. During energetic storm events in autumn and winter offshore significant wave heights can become over 5 m with storm surges reaching ~1 m. The semi-diurnal tidal elevation is about ~1.5 m for neap tide, increasing to ~2.0 m at spring tide. A 4hr flood period corresponding with a 8hr ebb period makes the tidal curve asymmetrical The sediment size ranges from 250-350 μm in the intertidal zone with an seawrd fining trend towards 200 μm.
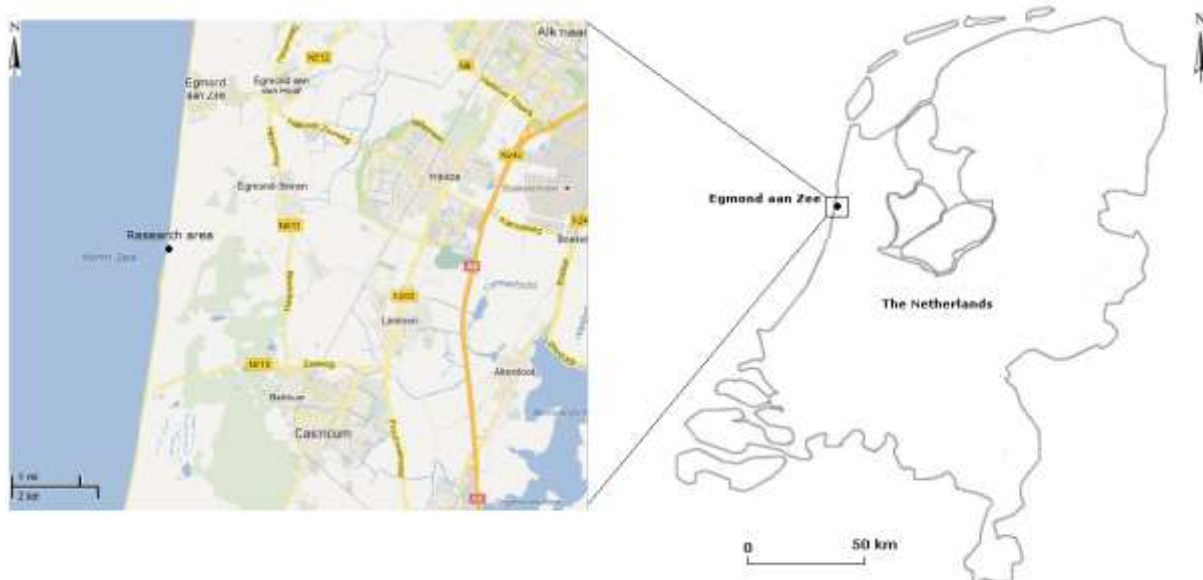
Figure 13 Location of the research area in Egmond aan Zee, the Netherlands.

The initial beach profile at 28 September is indicated with the solid line in figure 14 . The morphology, a typical summer profile, was characterized by an intertidal bar with a crest ~ 0.3 m above NAP and a seaward slope ~1:32, a berm with a crest of about ~1.6 m above NAP and a seaward slope ~1:11. The broken line shows the beach profile on 8 October. This is a typical winter profile that resulted from an autumn storm event of 4 days. It is clear the berm was destroyed. The intertidal bar moved seaward and was reduced in height now measuring ~0.1 m below NAP. Landward of the tidal bar a small through was visible only 0.3 m wide and 0.2 m deep. The seaward ward slope of the bar was ~1:30 and the slope landward of the through was ~1:27.
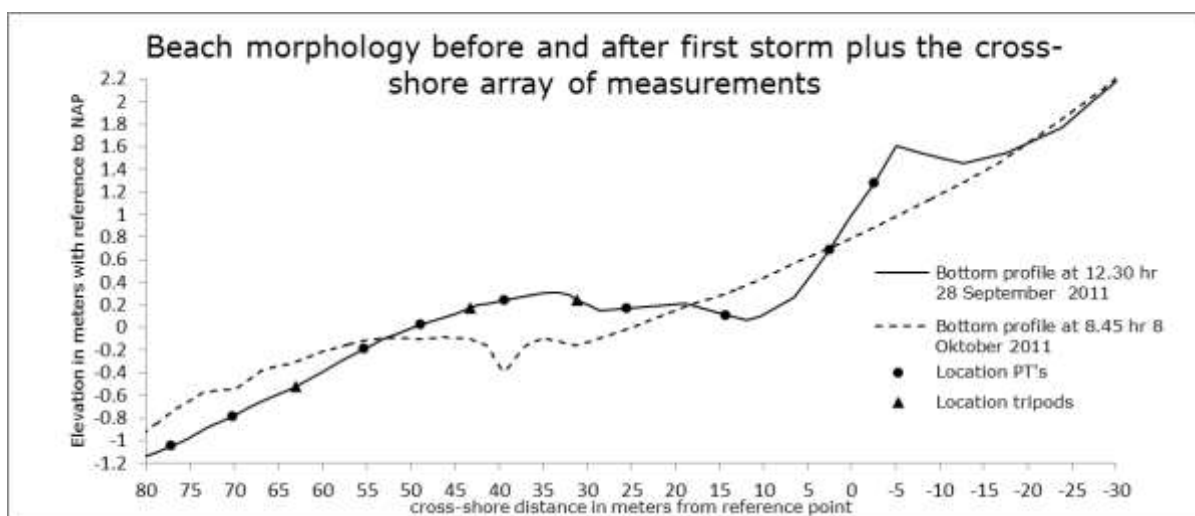
Figure 14, beach morphology and location of PT's and tripods

The data were collected in a cross-shore array of 12 instruments (3 tripods and 9 pressure transducers), also indicated in figure 14, plotted on the initial profile of 28 September . The tripods were positioned on the intertidal sand bar and included 3 optical backscatter sensors, 1 electromagnetic velocity meter (EMF) and 1 pressure transducer (PT). Figure 15 shows an overview of the array of instruments during low tide on 16 October.

Figure 15, picture of the instrument array and morphology at 16 October at 13.50

Figure 16 shows a schematic of the tripods, all the sensors and the data logger are indicated. The EMF sensor was located at a nominal height of 20 cm above the bed. The instrument height was defined as the height of the EMF sensor above the bed. The middle OBS sensor was aligned with the EMF sensor at the beginning of the field work period, to measures a nominal height of 20 cm as well. The lower and higher OBS sensors were set, at the beginning of the field work period, to 10 and 30 cm above the bed respectively.
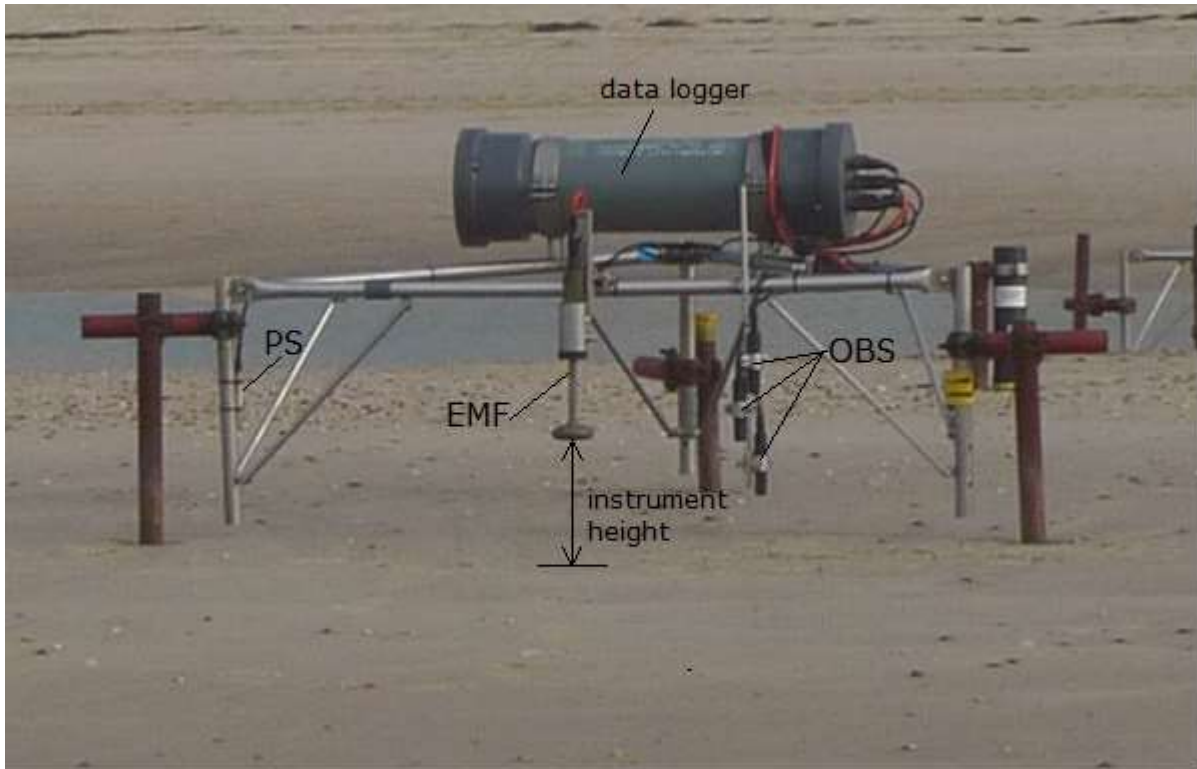
Figure 16, picture of the tripods with the measure devices and the data logger. Instrument height is also indicated.

Every other low tide the tripods were positioned so the EMF was at ~20 cm above the bed. Only if the instrument height was higher than 23 cm or lower than 17 cm, the instrument height was adjusted. In between every other low tide the instrument height fluctuated because of morphological change and the slow sinking of the tripods into the bed. Instrument height was measured every low tide before possible adjustment. At the moment the lowest OBS got buried, its height is zero. The instrument height of the EMF sensor was then 10 cm above the bed. The burial events of the lowest OBS provided additional measures of instrument height besides the direct instrument height values measured during low tide. The instrument heights were calculated, for the beginning of every burst, by linear interpolation between the measured height of the instruments before adjustment and the adjusted height of the previous low tide measurement. The cross-shore bottom profile was measured every other low tide using Differential Global Positioning System (DGPS) on the location of the instrument array. Every measured profile was interpolated over cross-shore distance to get equal spacing between the points of the profile. The bottom profiles, at the beginning of every burst, were calculated by linear interpolation between the profiles over time.

All sensors attached to the tripods sampled at 4Hz and stored their data on a data logger in bursts of 15 minutes. The 9 PT's sampled at 5 Hz, linear interpolation was used to convert the pressure data of the PT's to and interval of 4 Hz. The pressure transducer data were corrected for barometric air pressure. Water depth (h) per burst is defined as the mean of the pressure data. The pressure data was corrected to sea surface elevation using linear wave theory. OBS-sensors were calibrated using a recirculation tank with sand from the tripod locations, to derive the SSC in gr/L. The EMF sensor recorded velocity in m/s in a cross-shore and alongshore direction in the vertical plane. For velocity measured in the cross-shore direction (u) positive velocity values indicate landward directed flow while negative velocity values indicate seaward directed flow. For the alongshore velocity direction (v) positive velocity values equal north-ward directed flow and negative velocity values equal south-ward flow. The wave angle (α) is determined using Principal component Analysis of the gravity frequency filtered [u v] matrix. The wave angle is defined as the angle of the first eigenvector relative to normal. The mean wave period was calculated by dividing the inverse of the first-order spectral moment by the zeroth-order spectral moment (Tm-10). The settings for the spectral analysis are the same as explained in section 3.3.

Offshore wave heights and periods were obtained from the Stroommeetpaal IJmond, a location 14 km south of the research area and 2.5 km off the coast, at a water depth of ~12m. The offshore root-mean-squared wave height during the field work period was 0.10 m - 2.68 m and the offshore period ranged from 3.2 s – 9.6 s. Tidal data was available at IJmuiden Buitenhaven (14km south of the research area approximately at coastline in the IJmuiden Harbor) and at Petten Zuid (20km north of the research area and 500m of the coast). The water levels relative to NAP at the research area were estimated to be the mean of the IJmuiden Buitenhaven and Petten Zuid data.

3.2 Data screening

Pre-processing was required, prior to data analysis, to reject incomplete or unsuitable time series. For further analysis bursts 30 minutes in length were used. Pre-processing included the variables: cross-shore velocity, alongshore velocity, pressure and suspended sediment concentration. The SSC data from the lowest sensor was considered for analysis. Only if the data from the lowest OBS was rejected the middle OBS data was used. Instrument height of the lowermost OBS sensor measured 11.7 cm on average with a standard deviation of 5.7cm.

Simple algorithm was written to force time series per burst to be NaN for all instruments when the following conditions were satisfied:

- If the velocity or pressure data contained more than 10% zero values or NaN. It often occurred that the float was buried in sand, resulting in data collection during low tide. During low tide the sensors on the tripods emerged, leading to incomplete or empty data sets. Also the Burial of the EMF sensor or one of the OBS sensors led to saturation of the sensors and therefore to zero values in the sensor data.
- If only the lowest OBS data contained 10% zero values or NaN, the data remained unchanged. The middle OBS is than considered for analysis. When the SSC data of the middle OBS also contained 10% zero values or NaN, the time serie data for all instruments is set to NaN.
- If the SSC data of the lowest OBS contained less than 20 SSC peaks larger than 10 g/L or had a mean SSC exceeding 20 g/l, the middle OBS is considered for analysis. When the SSC data of the middle OBS also contained less than 20 SSC peaks larger than 10 g/L or had a mean SSC exceeding 20 g/l, the time serie data for all instruments is set to NaN. This condition ruled out bursts with close to no transport and the bursts with extremely large values which indicate almost complete burial of the sensor.

After the exclusion of data according to the described method above, all remaining series were visually inspected for spikiness, anomalies or signs of burial. Unexpected spikiness has occurred in the records of a malfunctioning pressure sensor of one of the tripods in the beginning of the research period. Anomalies occurred for instance in the velocity record, when the wave induced oscillations suddenly were absent from the record.

Signs of burial included the sudden increasing trend to very large SCC values, long non-wave related events of large SSC values and moments of sensor saturation. Bursts with velocity or pressure data containing spikiness, anomalies or signs of burial were rejected. If the lowest OBS sensor contained spikiness, anomalies or signs of burial the middle OBS was considered for analysis. When the middle OBS sensor also contained spikiness, anomalies or signs of burial the burst was rejected for analysis.

By means of the selection procedure a total of 384 bursts were selected. For the most landward tripod mostly, located in the inner surf zone, 59 burst were selected. A number of 87 bursts were selected for middle tripod, located in the middle part of the surf zone. Finally the most seaward tripod, dominantly located in the outer surf zone, produced 238 bursts after selection.

3.3 Data processing

All 384 bursts remaining after the data screening are included in the data processing. The data set was first used to analyse which factors determine the importance of infragravity wave to gravity waves within the surf zone. For the calculation of the importance of IG waves compared to gravity waves (IG_{imp}) eq.2 is used:

$$IG_{imp} = \frac{H_{rmsIG}}{H_{rmsG} + H_{rmsIG}}, \tag{2}$$

where H_{rmsIG} is the root-mean-squared IG wave height and H_{rmsG} the root-mean-squared gravity wave height. A value for IG_{imp} of 0.5 indicates equal importance of the IG waves compared to the gravity waves, a value for IG_{imp} of 1 implies that only IG waves are present in the SSE time series and a value of 0 would mean no IG waves are present in the SSE time series.

H_{rmsG} and H_{rmsIG} can be derived using power spectral analysis. The power spectral density is the power as a function of frequency. Plotting of the power spectral density of the SSE time series against frequency indicates which wave frequencies are dominating the SSE time series. For the calculation of the spectral densities, blocks of 5 minutes length with an overlap of 50% were used, this equals 11 blocks for a series of 30 min and a spectral resolution of 0.0033 Hz . The blocks are tampered with a Hamming window of 5 min length. Windowing improves the fourier analysis by forcing the signal at the ends of all block to be zero eliminating the contribution of the signal near the ends of the blocks.

Considering the window and block size used, series of 30 min measure 15 degrees of freedom and an upper and lower confidence interval of 62,98% and 182,91% respectively . Based on the Rayleigh distribution the H_{rmsG} and H_{rmsIG} can be calculated with eq. 3 and 4 respectively.

$$H_{rmsG} = 2\sqrt{2}\sqrt{\int_{f_1=1}^{f_2=0.05} Sxx(f)df}, \tag{3}$$

$$H_{rmsIG} = 2\sqrt{2}\sqrt{\int_{f_1=0.05}^{f_2=0.005} Sxx(f)df}, \tag{4}$$

where f_1 is the lower boundary and f_2 is the upper boundary of the integral, $Sxx(f)$ is the spectral density as a function of frequency. H_{rmsG} is calculated for f_1 is 0.05 Hz and f_2 is 1 Hz, whereas H_{rmsIG} is calculated for f_1 is 0.005 Hz and f_2 is 0.05 Hz.

The cross-shore location within the surf zone, offshore wave height and water depth are expected to be the most important factors influencing the IG_{imp}. To quantify the cross-shore location within the surf zone, a normalized distance parameter x_n was defined. The normalized distance parameter is expressed in eq. 5, as a ratio between the distance to shore and the total width of the surf zone:

$$x_n = \frac{x - x_s}{x_b - x_s}, \tag{5}$$

where x is the cross-shore location of the tripod compared to reference point, x_s is the cross-shore location of the coast line compared to reference point and x_b is cross-shore location of breakpoint of gravity waves compared to reference point. When $x = x_b$, $x_n = 1$, implying the burst is measured by a tripod located at the breakpoint of waves. For $x = x_s$, $x_n = 0$, the burst is measured by a tripod located at the coast line. For bursts measured by a tripod located within the shoaling zone holds $x > x_b$ and $x_n > 1$. For bursts measured by a tripod located within the surf zone $x_s < x < x_b$ so $0 < x_n < 1$. In practice the all 384 bursts were located within the surf zone with a maximum value for x_n of 1 and a minimum value of 0.25.

The per burst x_s was defined as the cross-shore location where the mean water level intersected with the cross-shore profile at the start time of the burst. Figure 14 shows an example of how x_s is determined. The mean water level (bold line) was calculated by taking the mean of the water levels per station (indicated with + sign) . A broken line with a cross on the x-axis indicates where cross-shore location of the intersect. If two points of intersection where found (usually when mean water level with reference to NAP was just below the top of the bar), the most seaward point of intersection was considered to be x_s.
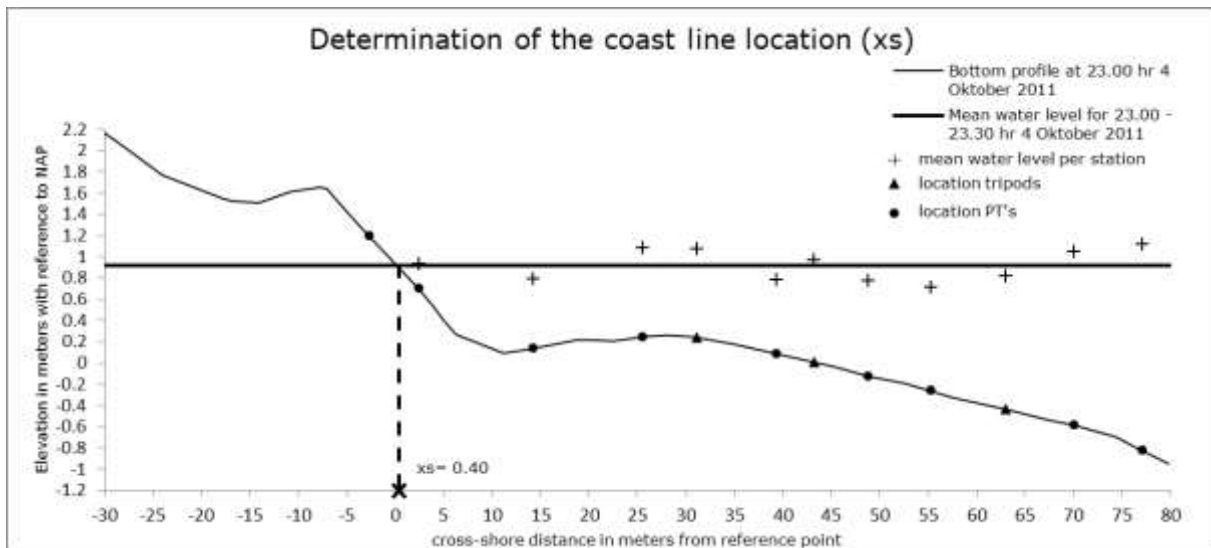
Figure 17, example of the determination of the coast line location (xₛ), where X marks the location coinciding with the intersect of the bottom profile and the mean water level

For the determination of x_b the spatial dissipation rate was determined using both the SSE data from the PT's and tripods. The spatial dissipation rate was considered to be equal to the spatial derivative of the wave energy flux (E_{flux}). The set of equations 7-14 are used to calculate the E_{flux} per instrument. In order to calculate the E_{flux}, the power spectral density of the SSE time series and the wave group velocity (c_g) need to determined, both as a function of frequency. Power spectral analysis is used to calculate power spectral density of the SSE time series as a function of frequency, using the same settings as for eq. 3 and 4. For the calculation of c_g the wave number k needs to be known. The value of k is usually calculated using the dispersion equation. Using linear wave theory the dispersion equation can be expressed as:

$$\omega^2 = gk \tanh(kh), \tag{6}$$

In which the angular velocity $\omega = 2\pi f$ and where ω squared relates to the wave number (k) times the hyperbolic tangent of k times the h. Since Eq. (6) is nonlinear in terms of k, k cannot be solved analytically.

By using the logarithmic matching method Guo (2002) proposed a solution for k. Applying the logarithmic matching Guo (2002) derived set equations, eq. 8-10 that were used to calculate k:

$$x = \frac{h\omega}{\sqrt{gh}}, \tag{7}$$

$$y = x^2 \left(1 - e^{-x^\beta}\right)^{-\frac{1}{\beta}}, \tag{8}$$

$$k = \frac{y}{h}, \tag{9}$$

where x is a dependant variable, h is the mean water depth, ω is the angular velocity, g is the gravitational acceleration, y is a dependant variable and β is a transitional shape parameter that is determined by a least-squares method to have value of 2.4908 (Guo, 2002). Eq. 10-12 show how the celerity (c) and wave group velocity (c_g), both in m/s, can be calculated:

$$c = \frac{2\pi f}{k}, \tag{10}$$

$$n = \frac{1}{2}\left(1 + \frac{kh}{\sinh(2kh)}\right), \tag{11}$$

$$c_g = cn, \tag{12}$$

where f is frequency, k is the wave number, h is the water depth and n is a dimensionless factor indicating the proportion of the celerity of individual waves to the wave group velocity. The value of n ranges from 0.5 in deep sea to a value of 1 in shallow water. Eq. 7-12 where calculated for the same f-values used in spectral analysis, for $1 \geq f \leq 0.005$ with an interval of 0.00033 Hz. The energy flux (E_{flux}) is calculated by integrating Sxx times c_g for the whole wave spectrum in eq. 13 and the dissipation rate (D) is calculated by the spatial derivative of the E_{flux}:

$$E_{flux} = g \int_{f_1=1}^{f_2=0.005} Sxx(f) * c_g(f)df, \tag{13}$$

$$D = \frac{dE_{flux}}{dx}, \tag{14}$$

where g is the gravitational acceleration, f_1 is the lower boundary and f_2 is the upper boundary of the integral, Sxx(f) is the spectral density as a function of frequency. For every burst the E_{flux} was calculated for all PT's and tripods. The E_{flux} in m^4s^{-3} is a measure of the energy carried along by waves. Figure 15 shows an example of x_b is determined. In figure 15A the E_{flux} values per station are plotted over the cross-shore distance, the dissipation of wave energy by wave breaking causes the E_{flus} values to decrease towards the coast line. The largest dissipation therefore occurs where the spatial gradient in E_{flux} is the largest. Dissipation (D), the spatial gradient in E_{flux} (D) in m^3s^{-3}, is thus a measure of wave dissipation and wave breaking.

In figure 15B the dissipation values per station are plotted over the cross-shore distance, the largest peak in negative dissipation was considered to be the breakpoint. A broken line with a cross on the x-axis indicates at what cross-shore location the largest peak in dissipation occurred. If the largest dissipation value occurred at location of the most seaward station, the location of the most seaward station was considered to be x_b.
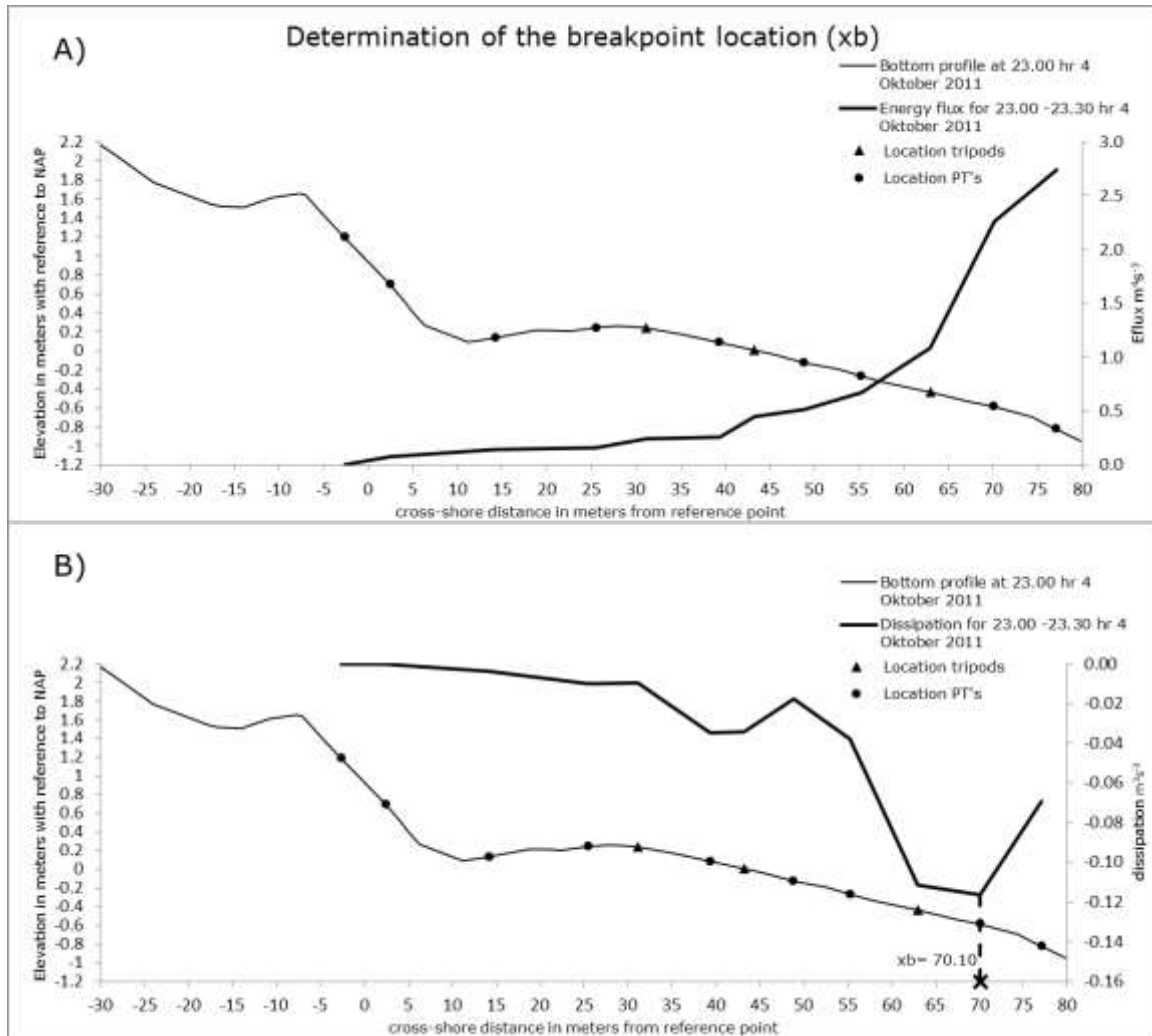
Figure 18, A) shows an example of the E_{flux} as a function of cross-shore distance compared to reference point. B) shows the corresponding dissipation values. The break location of waves (x_b) is marked X, corresponding to the location of the largest negative dissipation peak.

To analyse the SST per burst, the instantaneous SSC of the lowermost OBS sensor and instantaneous velocity of the EMF sensor was used for the three tripods. Total SST flux (q), the mass of sediment per unit surface and unit time, can be divided into two components (eq. 15):

$$q = q_{AV} + q_{wave} ,$$ (15)

the mean SST component (q_{av}) is the SST resulting from time-mean undertow current and the time-mean SSC . The SST component by waves (q_{wave}) is the SST due to instantaneous oscillatory velocity under waves and instantaneous second-order detrended SSC .

The q_{wave} can be separated into a gravity and IG component (eq.16):

$$q = q_{AV} + q_G + q_{IG}, \tag{16}$$

Where q_G results from the gravity frequency filtered instantaneous velocity and SSC series and q_{IG} results from the IG frequency filtered instantaneous velocity and SSC series

Total SST flux (q) is defined in eq. 17 as:

$$q = \langle u\, c \rangle = \langle \bar{u}\, \bar{c} \rangle + \langle \tilde{u}_G \tilde{c}_G \rangle + \langle \tilde{u}_{IG} \tilde{c}_{IG} \rangle, \tag{17}$$

where q is time-averaged, denoted with $\langle\,\rangle$, product of the instantaneous velocity (u) and the instantaneous SSC (c) series. The mean component, $\langle \bar{u}\, \bar{c} \rangle$, is the time-averaged product of the mean velocity ($\bar{u}$) and the mean SSC ($\bar{c}$). The gravity wave component, $\langle \tilde{u}_G \tilde{c}_G \rangle$, is the time-averaged product of the $\tilde{u}_G$ and $\tilde{c}_G$. Where $\tilde{u}_G$ and $\tilde{c}_G$ are the second-order detrended and high-pass-filtered (range 1-0.05Hz) series of u and c respectively. The IG wave component, $\langle \tilde{u}_{IG} \tilde{c}_{IG} \rangle$, is the time-averaged product of the $\tilde{u}_{IG}$ and $\tilde{c}_{IG}$. Where $\tilde{u}_{IG}$ and $\tilde{c}_{IG}$ are the second-order detrended and low-pass-filtered (range 0.05-0.005Hz) series of u and c respectively . All SST fluxes are given in units kg m^{-2}s^{-1}.

To determine the presence of the different IG frequency SST mechanisms as a function of x_n three approaches were used:

- Time series of SSE, velocity and SST were plotted and visually analysed for bursts with different values of x_n to determine the IG frequency SST mechanisms.
- The Pattern of IG frequency SST as a function of x_n of all bursts was used to determine which IG frequency SST mechanism was most likely active for which x_n values
- For every burst the wave envelope of the gravity SSE and the gravity velocity time series were calculated using the Hilbert Transform operation. A wave envelope is a smooth curve outlining the extremes in amplitude. The correlation of the SSE or velocity wave envelope with the IG frequency filtered SSE or velocity time series is a measure of the modulation of gravity waves by IG waves. Where a positive correlation between the gravity velocity wave envelope and the IG frequency filtered velocity indicates that gravity waves have larger velocity amplitudes during onshore directed part of IG waves. Negative correlation between the gravity velocity wave envelope and the IG frequency filtered velocity indicates that gravity waves have larger velocity amplitudes during offshore directed part of IG waves.

4 Results

4.1 Boundary conditions

The field campaign was characterized by varying hydrodynamic conditions and changes of the intertidal beach morphology. The hydrodynamic conditions are discussed in this section and the morphological change during the same periods is discussed in the next section. In figure 19 A-D offshore root-mean-squared wave height, wave period, wave angle and the measured and astronomical tidal elevation are showed. Based on the hydrodynamic boundary conditions and in particular the offshore wave height, five different periods (three calm periods and two storm periods) are defined:

- Period I: the first period, from 28 September till 3 October was characterized by a H_{off} measuring ~0.2 m, with during 3 October an increase up to ~1 m at the end of the day. The wave period fluctuated ranging between 4-6 s. The wave angle ranged from about 160º - 300º, S to NW. Measured and Astronomical Tidal elevations were quite similar with a tidal amplitude at the start of the periode of 2.1 m evenly decreasing to a tidal amplitude of 1.7 m at the end of the period

- Period II: from 4 October till 11 October, was the first storm period, interrupted by one calm day on 9 October. At the start of 4 October H_{off} ~1.0 m increasing up to ~2.6 m at the end of 6 October. The H_{off} drops to ~0.8 m at the beginning and ~1.0 m at the end of 9 October. On 10 and 11 October H_{off} measures ~2.2 and ~2.3. The wave period increased from ~5 s to ~7 s from 4 to 6 October. On 7 and 8 October the wave period remains ~7 s. On 9 October the wave period dropped to ~5 s. The wave period was ~6 s again on 10 and 11 October. The wave angle was ~230º SW for 4 and 5 October. On 6 October the wave angle changed to 330º NW for 7 and 8 October. The wave angle changed again to ~230º SW for 9,10 and 11 October. The tidal amplitude on 4 October of ~1.5 m evenly decreased to a tidal amplitude of ~0.8 m on 6 October increasing again towards ~1.6 on 11 October. The measured tidal elevation was ~0.3m higher for 4, 5, 10 and 11 October and 0.4-0.8 m higher on 7 and 8 October. This set-up due to storms is known as storm surge.
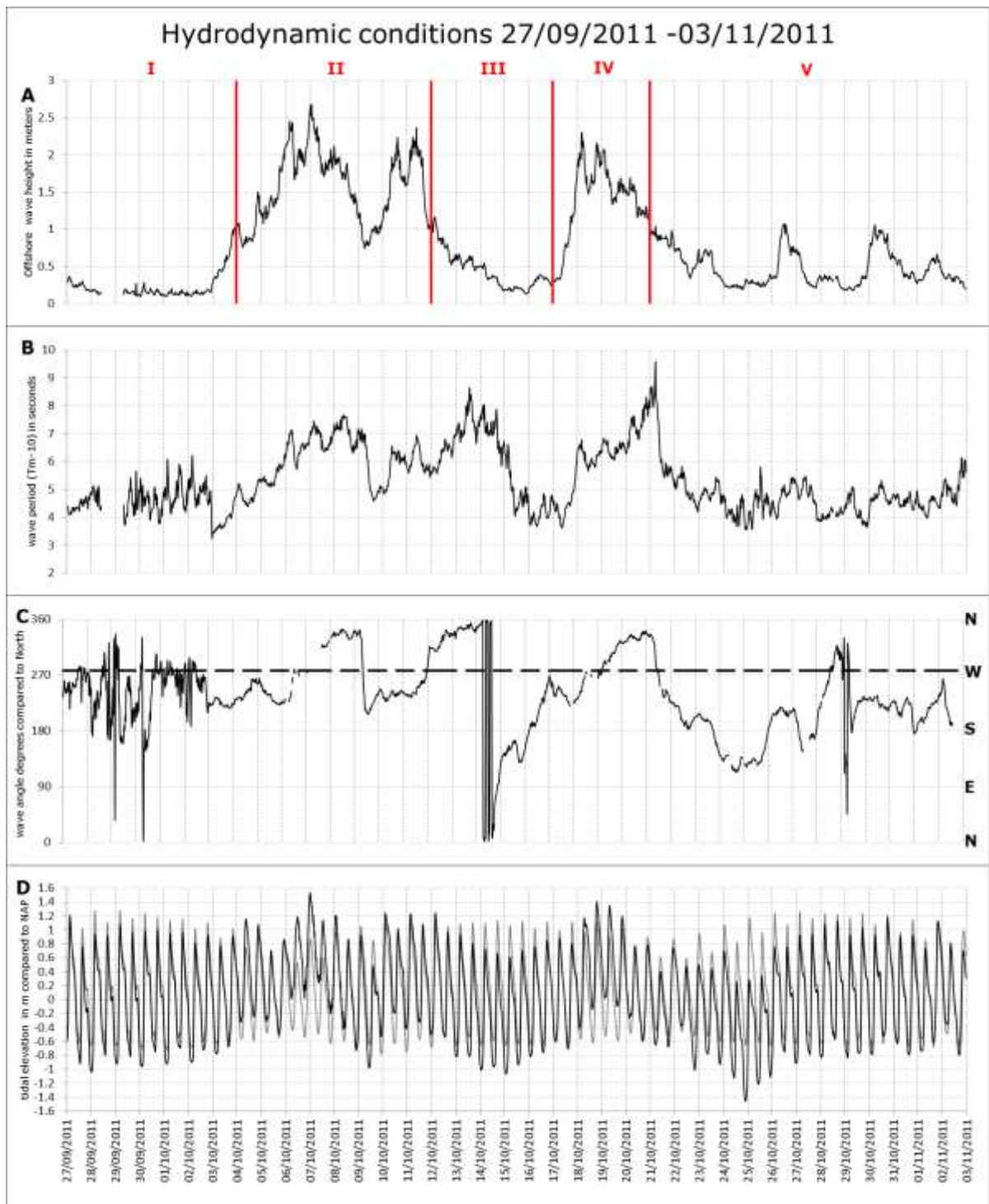
Figure 19, boundary conditions for the total field work. A) Offshore root-mean-squared wave height, were I-V indicate five different time periods. B) Total wave period in sec (T_{m01}) C) wave angle in degrees compared to the North. The angle of waves perpendicular to the coast line (277° W) are indicated with a broken line D) Tidal elevation, with the black line indicating the measured tidal elevation and astronomical elevation.

- Period III: was the second calm period, from 12-16 October. During this period the H_{off} gradually decreased form ~1.0 m at the beginning of the period towards ~0.3 m at the end of the period. On 12 October the wave period increased from ~6 s to ~8 s. The wave period on 13 and 14 October remained 8 s, and dropped again to 4.5 s on 15 and 16 October. The wave angle on 12 October of ~310º W shifted to ~340º N on 13 and 14 October. From 14 to 16 October the wave angle changed evenly to ~160º S on 15 October and ~270º W on 16 October. The tidal amplitude gradually decreased from ~1.7 m at the beginning of the period to ~1.4 at the end of the period. Measured tidal elevation was ~0.3 meter lower for 13 October and ~0.4 meter lower for 14 October. For 15 and 16 October the measured tidal elevation was ~0.5 m lower.

- Period IV: from 17-20 October, the second storm period, was characterized by: a rapid increase in H_{off} for on 17 October, a H_{off} measuring ~2.0 m on 18 October and a H_{off} gradually decreasing to ~1.5m and 1.0 m on 19 and 20 October respectively. The wave period increased from ~4 to ~6.5 s on 17 October. On 18 and 19 October the wave period remained ~6.5 s. The wave period peaked with ~8 s on 20 October. The wave angle on 17 October was ~270º W, turning to ~230º SW at the end of 18 October. From the beginning of 19 October towards the end of 20 October, the wave angle changed from~230º SW to 330º NW. Tidal amplitude gradually decreased from 1.6 mat the beginning of the period to 1.4 m at the end of the period. On 18 and 19 October the storm surge measured ~0.5m.

- Period V: was the third calm period from 21 October to 3 November. The H_{off} varied between ~0.3 and ~ 1.0 m, the wave period was ~4.5 s. The wave angle was mainly directed ~220º SW. With the exception of 24 and 25 October (120º SE) and 28 October (300º NW). The tidal amplitude varied between 1.1 to 1.8 m. The measured tidal elevation was smaller than the astronomical tidal elevation for 23 to 26 October measuring ~0.4 m, ~ 0.6 m, ~0.9 m and 0.4 m respectively.

The tripod locations within the surf zone, the x_n values per tripod, varied during the research period. For the most seaward tripod was x_n was on average ~0.89 with a standard deviation of 0.06. The middle tripod was located at x_n ~0.61 with a standard deviation of 0.05. The most landward tripod is located on x_n ~0.41 with a standard deviation of 0.07. To get an indication of the mean tripod locations compared to the morphological profile. The x-value of the bar crest, defined as cross-shore location of the bar crest compared to reference point, was calculated. The x_n value was determined by eq. 5. The mean x_n value of the bar crest was 0.56 with a standard deviation of 0.15. This indicated that the seaward tripod was located on the seaward slope of the bar, just landward of the breakpoint of waves, during the whole fieldwork period. The middle tripod was mostly located on the top of the bar, just seaward from the bar crest. The middle tripod was occasionally located just landward of the bar crest in the through. This was also visually validated during the field work. The landward tripod was predominantly located in the through landward from the bar crest.

Hydrodynamic variables are calculated for the selected set of bursts. In figure 20 the distribution of these variables, number of bursts per category, is plotted. The key figures and the distribution plots are discussed per variable. H_{off} is shown in figure 20 A, with an minimum value of 0.44 m, an average of 1.61 m and a maximum value of 2.68 m. Only 11.4 % of the bursts had an H_{off} value of lower than 1 m. This means that most of the bursts selected, were collected during the storm period II and IV. The distribution of water depth in figure 20 B, indicates that a water depth of 0.6-0.8 m was measured for most bursts. The average water depth was 1.03 m, minimum water depth was 0.44 m and the maximum water depth was 2.09 meter. H_{rmsG} and H_{rmsIG} on the tripod location were plotted in figure 20C and 20D, and measured 0.30 and 0.16 m on average. The H_{rmsG} ranged between 0.08 and 0.61 m and H_{rmsIG} ranged between 0.04 and 0.30 m. The total wave period (T_{m-01}) distribution, showed 20E, was 6.28 s on average with a minimum period of 3.14 s and a maximum period of 10.3 s. The wave angle compared to shore normal is plotted in 20F, were 0º is normal to shore, wave angel >0º indicate oblique wave waves from the S-SW and wave angel < 0º indicate oblique wave waves from the N-NW. The wave angle was 3.5º on average and ranged from -11.4º to 21.0º. When calculating H_{rmsG}, $H_{rmsIG,}$ and gravity or IG filtered velocity or SSE time series, the assumption is made that wave angle is not far from coast normal . This assumption is justified, a wave of 21.0 would only reduce actual wave height, gravity and IG filtered SSE and velocity by ~7%.

The cross-shore and alongshore mean velocity distributions are showed in figure 20G and 20H respectively. The mean cross-shore velocity was always offshore directed, with a mean velocity of -0.20 m s^{-1}. The mean cross-shore velocity ranged from 0.00 m s^{-1} to -0.42 m s^{-1}. The alongshore current values ranged from -0.92 m s^{-1} to 0.79 m s^{-1}, with an average of 0.03 m s^{-1}. The negative alongshore current values indicate currents directed South and positive alongshore current values indicate currents directed North. Although this paper focusses on the cross-shore transport, alongshore mean transport values are expected to be of the same magnitude, if not exceed, the cross-shore mean transport values. While the mean cross-shore SST is only seaward directed, the alongshore current is directed both to the North (positive values) and the South (negative values), leading to both Northward and Southward directed mean alongshore SST. The large suspected mean alongshore SST is consistent with observations of alongshore variability in Morphology, namely the Northward and Southward shifting of intertidal bars intersected by rip-currents.
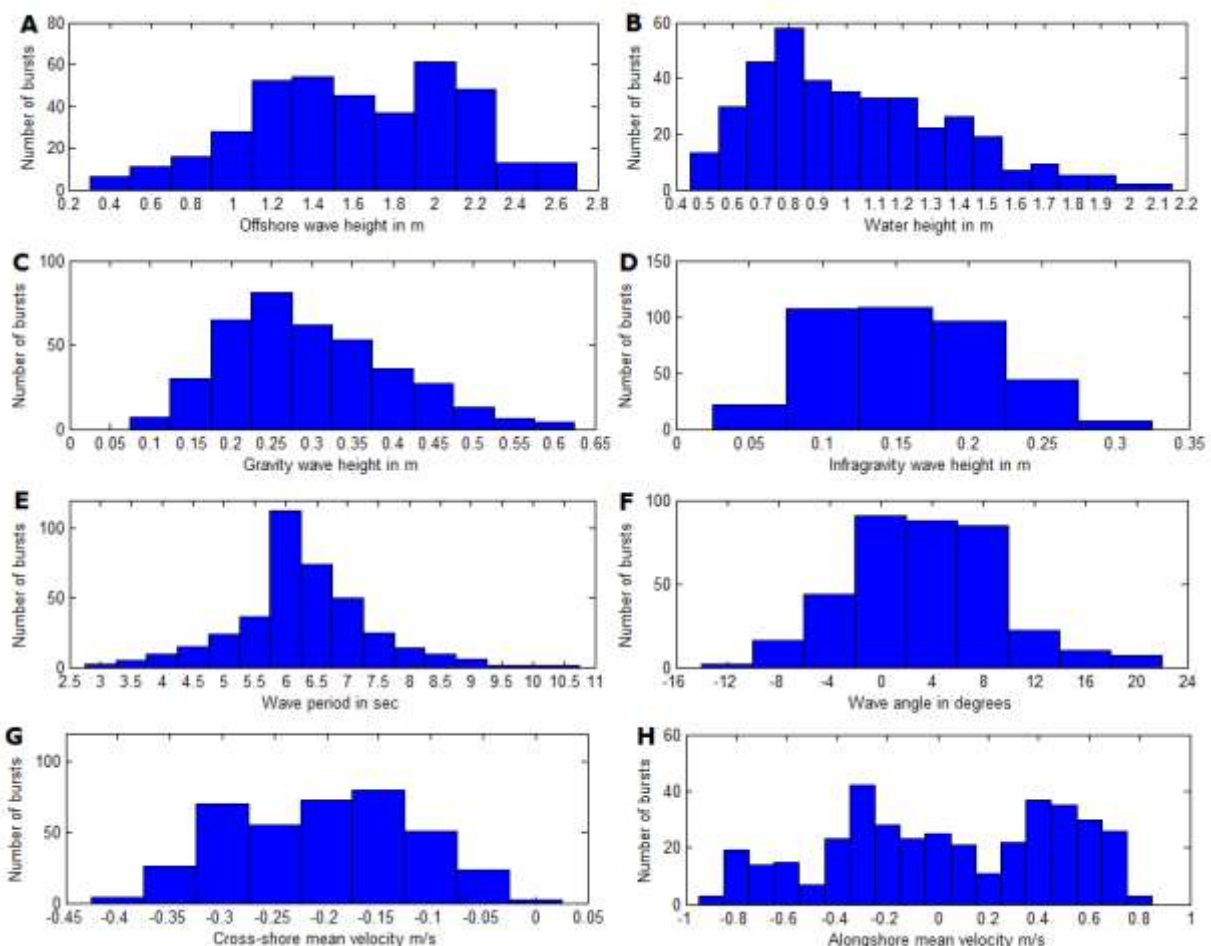
Figure 20, distribution plots of 8 hydrodynamic variables. Where the number of bursts are plotted per category. A is the distribution of Offshore root-mean-squared wave height. B is the distribution of water depth. C and D show the distribution of gravity and IG root-mean-squared wave height, E shows the distribution wave period and F the wave angle compared to shore normal. G and H show the distribution of the mean cross-shore and alongshore velocity respectively.

4.2 Morphological evolution

The morphology changed during the research period as a consequence of changing hydrodynamic conditions. The morphological changes are discussed using the same periods I-IV as were used to discuss the hydrodynamic conditions. Figure 20 shows profiles of period I-III and figure 21 shows the profiles of period IV and V. Period I-V where characterized by:

- Period I: the first calm period, from 28 September till 3 October, is indicated in figure 20 I. Period I was characterized a stable non-varying morphology. The profiles were characterized by an intertidal bar on x =35, with a crest of ~ 0.35 m above NAP and a seaward slope ~1:32. A berm was present at x=-5, with a crest of about ~1.6 m above NAP and a seaward slope ~1:11.

- Period II: indicated in figure 20 II during the first storm period. The profile of 4 October was similar to the profiles of period I. The crest of the intertidal bar was now located on x=30, measuring ~0.25 m above NAP with an seaward slope of ~1:41. The berm was still located at x=-5 measuring 1.7 m in height. The profile of 8 October showed, the berm was destroyed. The intertidal bar moved seaward to x=52 and was reduced in height, now measuring ~0.1 m below NAP. Landward of the tidal bar a small through is visible only 0.3 m wide and 0.2 m deep. The seaward slope of the bar was ~1:27. The slope landward of the through was ~1:25. On 9 October the bar moved landward to x=49 with a height of ~0.1 m above NAP. At the end of the storm period on 11 October the bar moved seaward again to x=52 with a height of ~0.1 m below NAP. The seaward slope of the bar remained ~1:27.

- Period III: was the second calm period, from 12-16 October. The profiles of 12, 14 and 16 October are shown in figure 20 III. On 12 October the bar measured ~0 m compared to NAP in height and was located at x=56. The profile of 14 and 16 October show the intertidal bar crest moved landward to x=45 with a height of ~0.2 m. A small berm (0.1 – 0.2 m high) started to reform at x=2. The seaward slope of the bar was ~1:27.
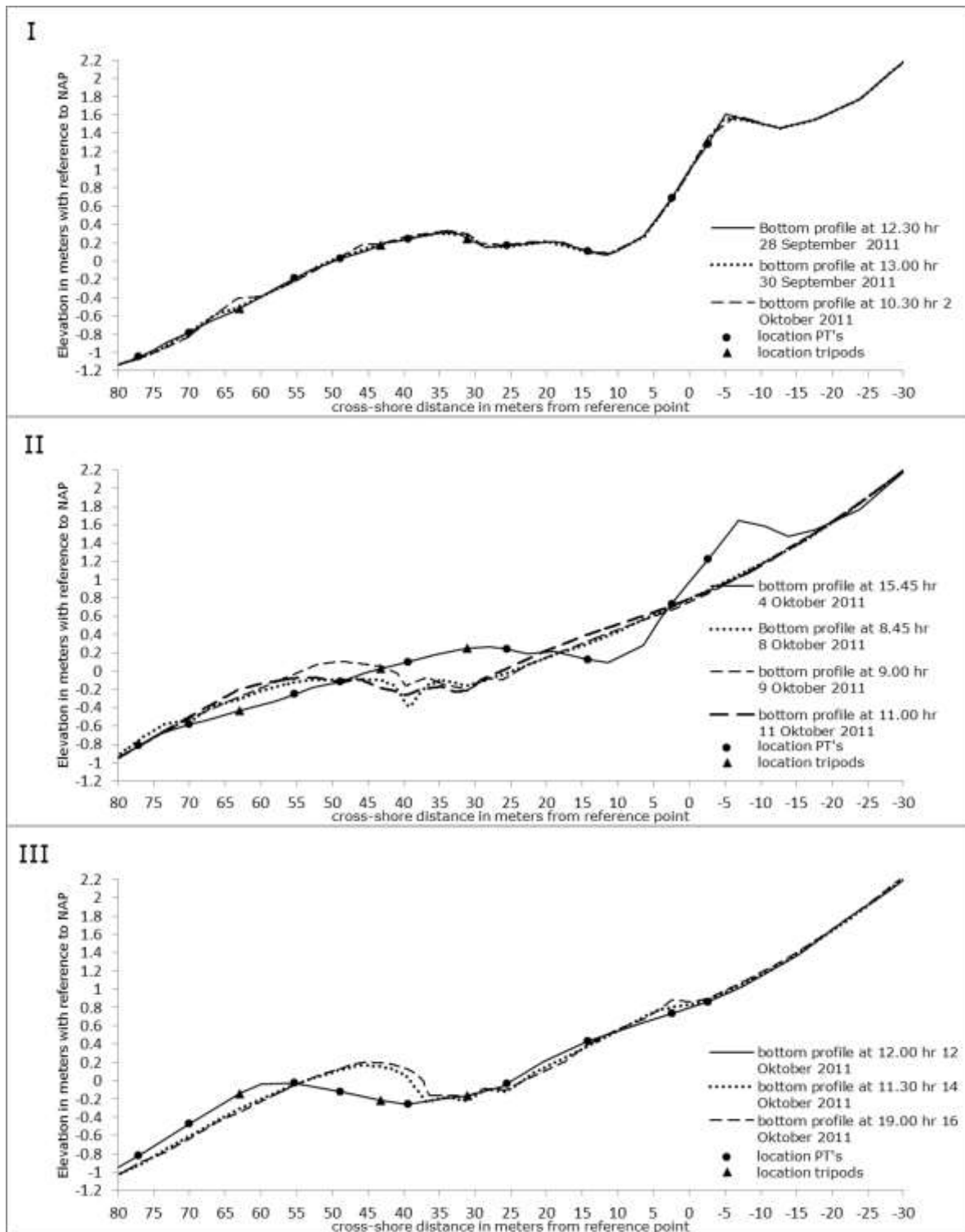
Figure 21, cross-shore bottom profiles at the location of the array of pressure transducers and tripods, for period I,II and III.

- Period IV: from 17-20 October, the second storm period, is shown in figure 21IV. the first profile of 17 October was quite similar to the end of period III. The intertidal bar crest was located at x = 42 and measured ~0.2 m compared to NAP. The seaward slope of the bar was ~1:30. The small berm moved seaward to x=10. The profiles of 19 and 20 October were quite similar. No berm was visible anymore. The Intertidal bar crest lowered to ~0 m compared to NAP and moved onshore to x=40. The bar also flattened with a slope of ~1:37.

- Period V: is the third calm period from 21 October to 3 November. The profiles of 21, 25 and 31 October are shown in figure 21 V. The bar crest moved landward to x=46, with a height of ~0.2 m above NAP, on 21 October. The seaward slope is ~1:30. Some small variations in the height and location the intertidal bar occurred in the rest of the period. On 25 October, the intertidal bar crest moved to x=41 with a height of ~0.1 m. At x=61 a small rip current was formed. On 31 October, the intertidal bar crest was located at x=49 with a height of ~0.3 m. The small rip current now moved Northward, but is still visible at x=45.
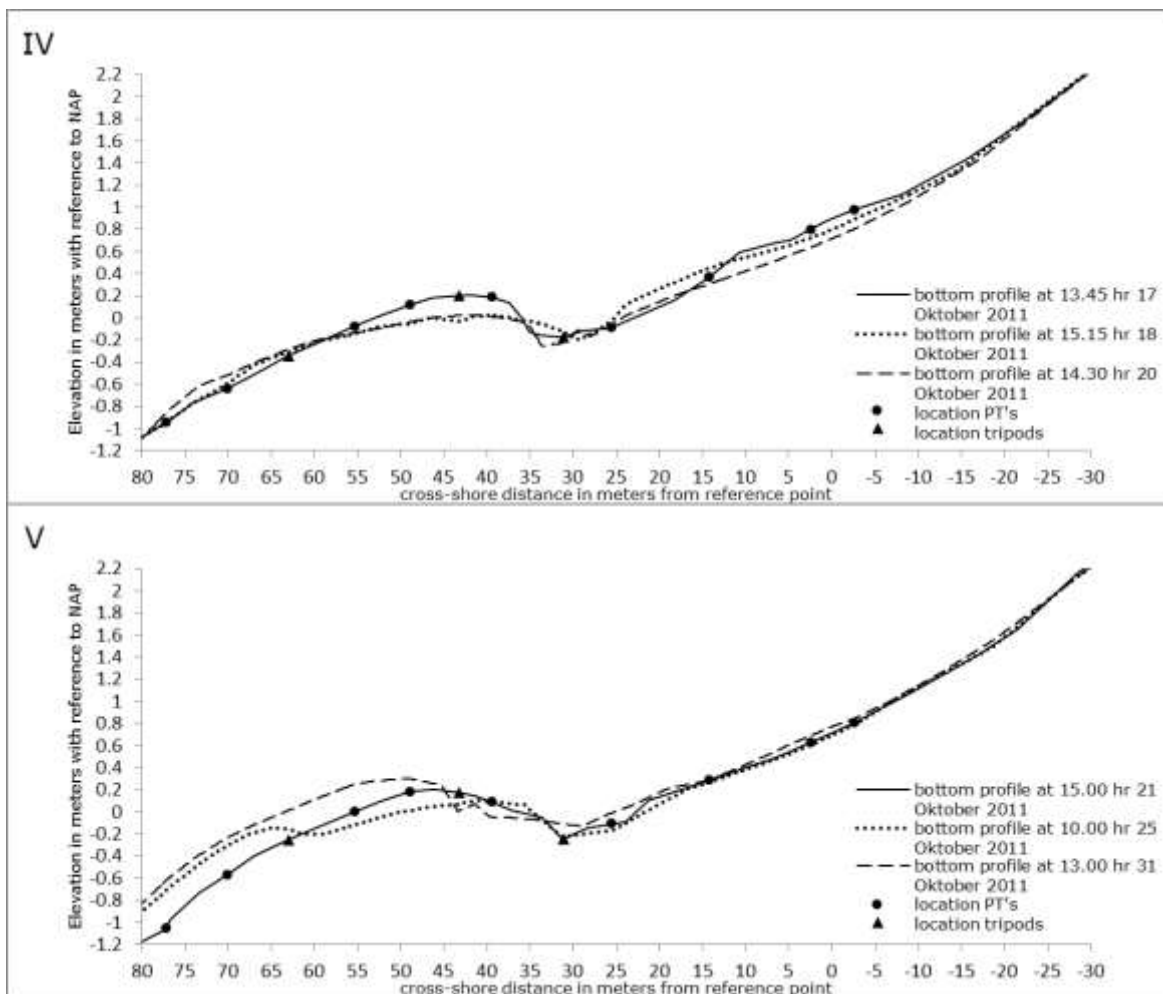
Figure 22, cross-shore bottom profiles at the location of the array of pressure transducers and tripods, for period IV and V.

In general the two storm events (period II and IV), with Ho > 1 m, destroyed existing berms by eroding the top and deposition in the trough at the base of the berm. The slope was reduced and the morphology smoothened. The second calm period the berm started to reform but got eroded again in the second storm period. The storm periods also caused erosion of the intertidal bar, the bar crest systematically moved seaward (x = 50-55) and reduced in height compared to NAP (~0.1 below NAP). Also the slope seaward of the bar generally got smaller during the storm periods (~ 1:40). Even around 9 October in period II, the H_0 dropped to ~1 m for around 24 hours, the intertidal bar crest also moved landward and heightened with 0.2 m compared to NAP.

4.3   Importance of infragravity waves

Both the normalized location within the surf zone, the offshore root-mean-squared wave height and the water depth related to the importance of infragravity compared to gravity waves. IG_{imp} is most significantly related x_n, with a R^2 of 0.5271. In figure 22 IG_{imp} is plotted against x_n for all bursts (indicated with the small crosses). A linear trend line based on all data points is indicated with a solid line. Black dots indicate the average IG_{imp} per category of x_n. Categories (x_c) are defined as $x_c - 0.05 < x_c \geq x_c + 0.05$, where x_c is (0.1;0.2;0.3;0.4;0.5;0.6;0.7;0.8;0.9;1.0). The average of the x_n values and the average of the corresponding IG_{imp} values within this category is determined. Error bars indicate the standard error per category, calculated by $1.96 \frac{1}{\sqrt{n}} \sigma$, where σ is the standard deviation and n the number of measuring point per category. The wave spectrum at breakpoint was dominated by gravity waves where the $Hrms_{IG}$ made up 25-30% of the total Hrms. Towards the coastline the IG_{imp} increased, with the $Hrms_{IG}$ making up 50-55% of the total Hrms. The importance of IG waves in the wave spectrum is significantly increased from break point towards the coastline.
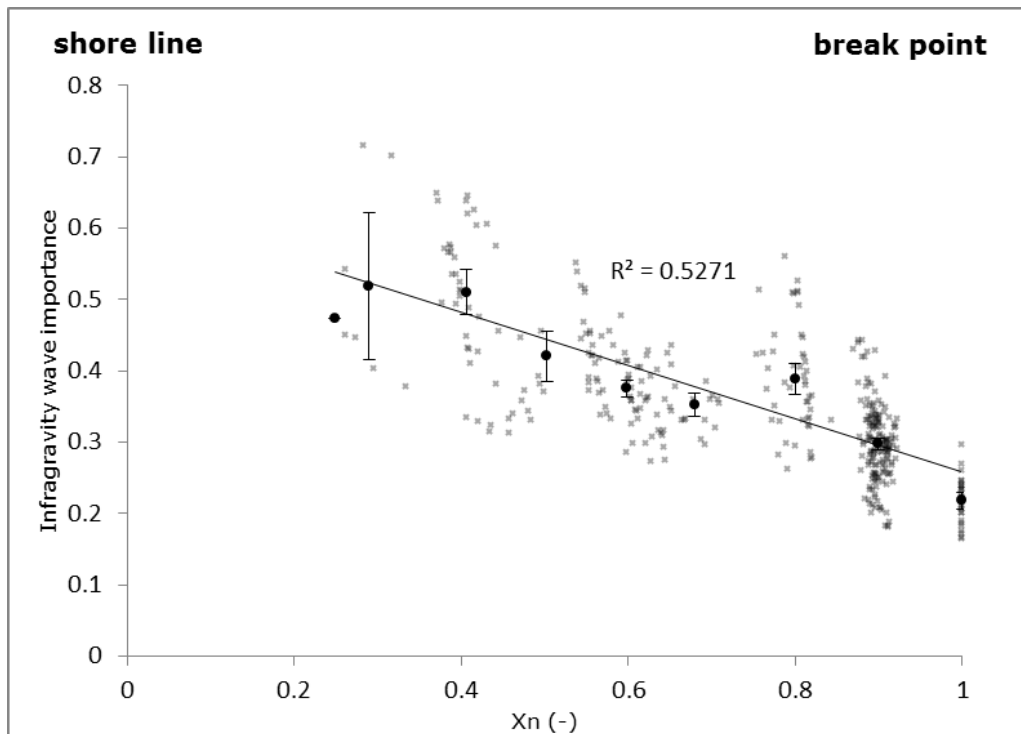
Figure 23, plot of IG$_{imp}$ against x$_n$, the crosses indicate the values for all bursts. Solid line indicates the linear trend line based on all data points. Black dots indicate the average IG$_{imp}$ per category of x$_n$ and error bars indicate the standard error per category. Indicated is also the shoreline, breakpoint and R^2 value.

H$_{off}$ and h were less significantly related to IG$_{imp}$ compared to x$_n$, with R^2 values 0.2586 and 0.0939 respectively. In figure 24 IG$_{imp}$ is plotted against H$_{off}$, where crosses indicated the measuring points and the solid line is the linear trend line. IG$_{imp}$ was positively related to H$_{off}$, meaning the IG$_{imp}$ increased with H$_{off}$. In figure 25 the relationship between h and IG$_{imp}$ is shown, where the crosses indicate indivual measuring points and the solid line shows the linear trend line. IG$_{imp}$ was negatively related to h, meaning the IG$_{imp}$ increased with decreasing h.

Incorporating the three parameters into one dimensionless parameter to better explain the sediment transport was not considered, for the three parameters are non-linearly related. The IG$_{imp}$ is best explained in terms parameter x$_n$, hence this parameter was used to explain the transport pattern.
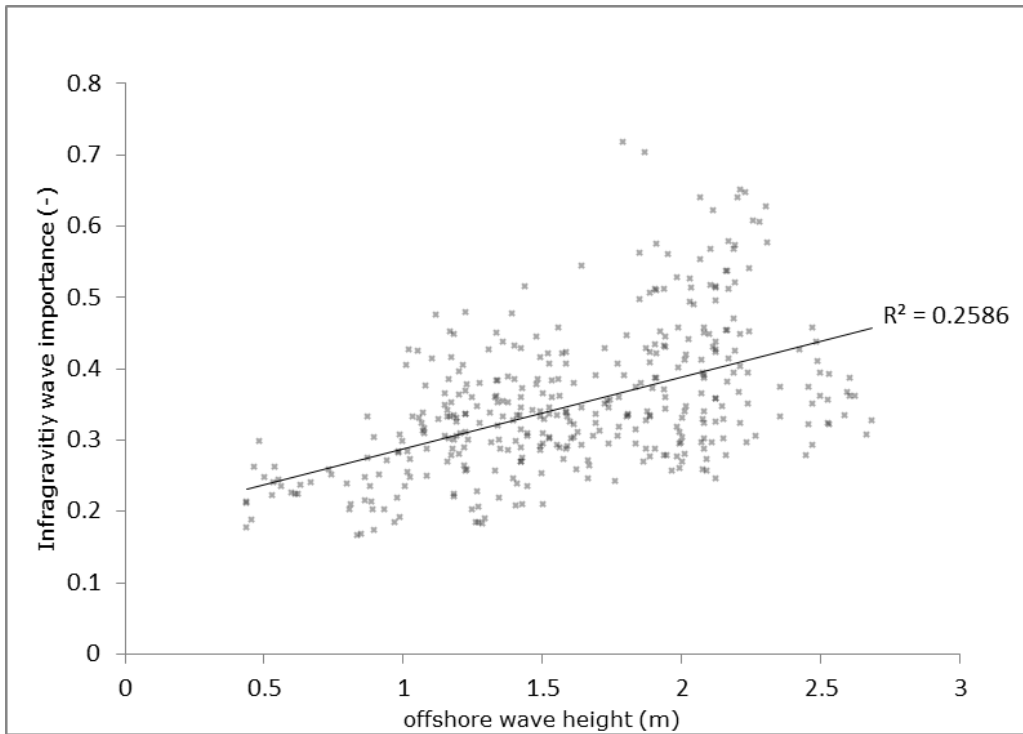
Figure 25, plot of IG$_{imp}$ against H$_{off}$, the crosses indicate the values for all bursts. Solid line indicates the linear trend line based on all data points, the corresponding R^2 value is also indicated.
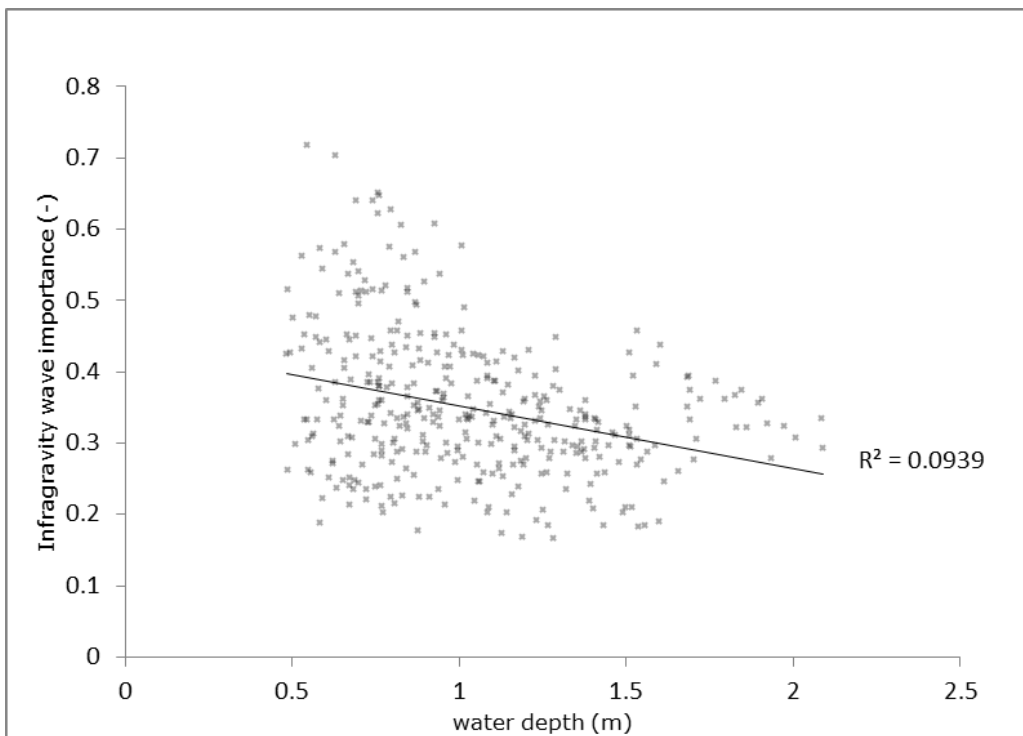
Figure 24, plot of IG$_{imp}$ against h, the crosses indicate the values for all bursts. Solid line indicates the linear trend line based on all data points, the corresponding R^2 value is also indicated.

4.4 Infragravity wave suspended sediment transport

In figure 26 the q_{IG} is plotted against x_n. The crosses indicate the data points for all bursts, black dots indicate the average q_{IG} against the average x_n per category x_c, and the error bars indicate the standard error per category. The q_{IG} was predominantly positive an thus landward directed, were the average q_{IG} per category decreased from 0.095 kg m^{-2} s^{-1} for x_n value of 0.9 to 0.018 kg m^{-2} s^{-1} for x_n value of 0.4 and 0.020 kg m^{-2} s^{-1} for x_n value of 0.3. Around breakpoint ($x_n=1$) the q_{IG} was -0.032 kg m^{-2} s^{-1},so seaward directed.
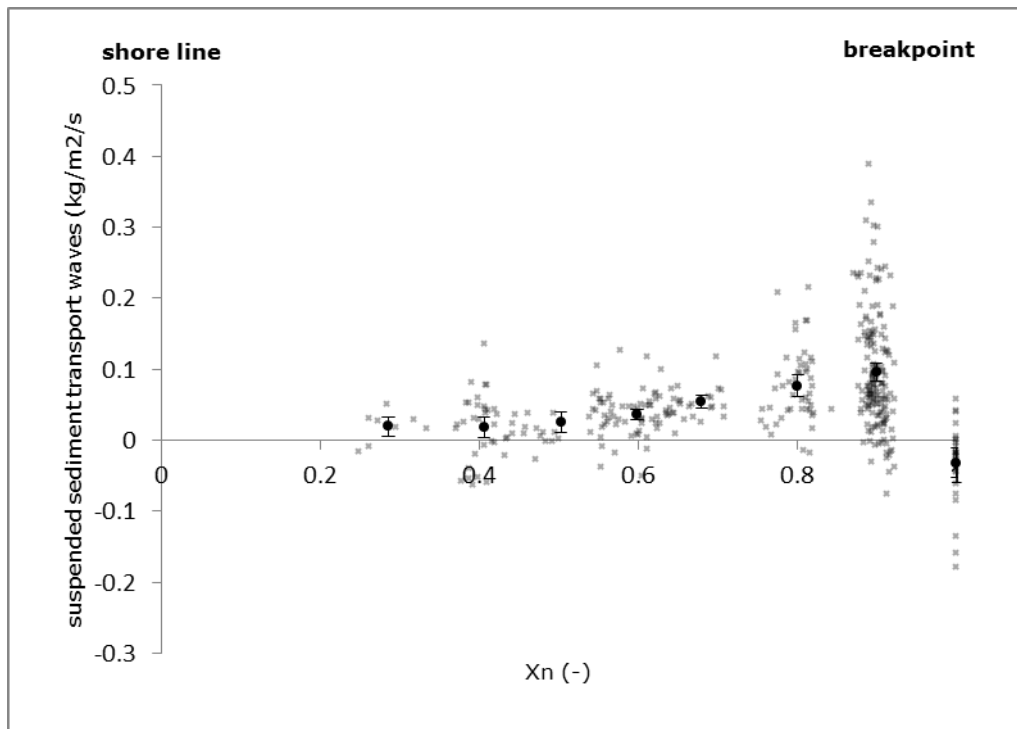
Figure 26, plot of q$_{IG}$ against x$_n$, the crosses indicate the values for all bursts. Black dots indicate the average q$_{IG}$ per category of x$_n$ and error bars indicate the standard error per category.

In figure 27 all transport components (q_{IG}, q_G, q_{AV} and q) were plotted as a function of average x_n per category x_c. When comparing the q_{IG} with the other transport components, q_{IG} proved to be comparable in magnitude to q_G. Highest value for q_G was 0.086 kg m^{-2} s^{-1}, decreasing landward until x_n= 0.6 with a value for q_G of 0.014 kg m^{-2} s^{-1}. More landward at, x_n = 0.3, q_G was higher with a value of 0.053 kg m^{-2} s^{-1}. At breakpoint (x_n = 1) the q_G is close to zero measuring only 0.006 kg m^{-2} s^{-1}.

The q_{AV} was seaward directed and proved to be higher than both q_{IG} and q_G for $1 > x_n < 0.4$. The maximum value of q_{AV} measuring -0.668 kg m^{-2} s^{-1} at $x_n = 0.9$, which was ~7 times higher than q_{IG} and ~8 times higher than q_G on the same location. The q_{AV} decreased towards to coastline with a value of -0.040 kg m^{-2} s^{-1} at $x_n = 0.3$. The value of q_{AV} measured -0.295 kg m^{-2} s^{-1} at break point. Because the q_{AV} was the largest component in almost the complete surf zone, q was also mostly seaward directed, with a maximum value at $x_n = 0.9$ of -0.493 kg m^{-2} s^{-1}. Only at $x_n = 0.3$ q was landward directed with a value of 0.024 kg m^{-2} s^{-1}.
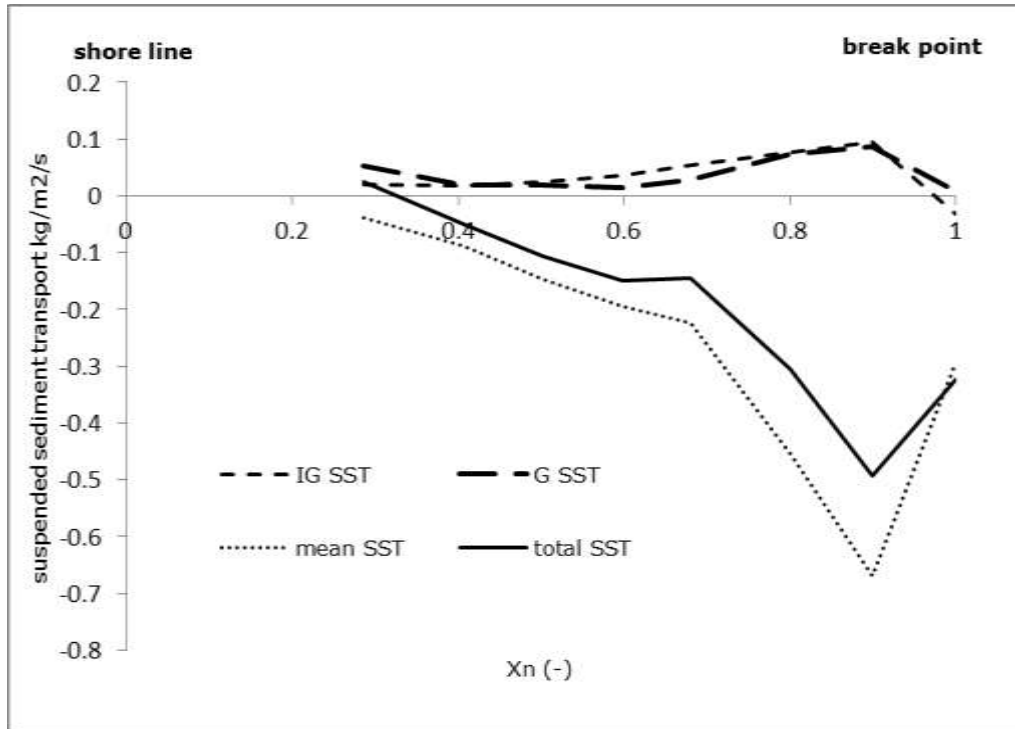
Figure 27, q_{IG}, q_G, q_{AV} and q plotted as a function of average x_n per category x_c.

Figure 28 shows q_{IG} plus the landward q_{IG}, seaward q_{IG} component of the q_{IG}. plotted as a function of average x_n per category x_c. To determine the landward q_{IG} the fomula for the IG wave SST component, $\langle \tilde{u}_{IG} \tilde{c}_{IG} \rangle$, was used. But before taking the average, all negative values in the series resulting by taking product of the $\tilde{u}_{IG}$ and $\tilde{c}_{IG}$ were set to nan. To determine the seaward q_{IG} the same fomula for the IG wave SST component, $\langle \tilde{u}_{IG} \tilde{c}_{IG} \rangle$, was used. And before taking the average, all positive values in the series resulting by taking product of the $\tilde{u}_{IG}$ and $\tilde{c}_{IG}$ were set to nan. Both the landward q_{IG} and seaward q_{IG} components have maximum values at $x_n = 0.9$ of 0.199 kg m^{-2} s^{-1} and -0.103 kg m^{-2} s^{-1} respectively. Both landward q_{IG} and seaward q_{IG} component decrease towards the coastline, were seaward q_{IG} component is always lower compared to the landward q_{IG} component. Only at breakpoint the seaward q_{IG} component exceeds the landward q_{IG} component.
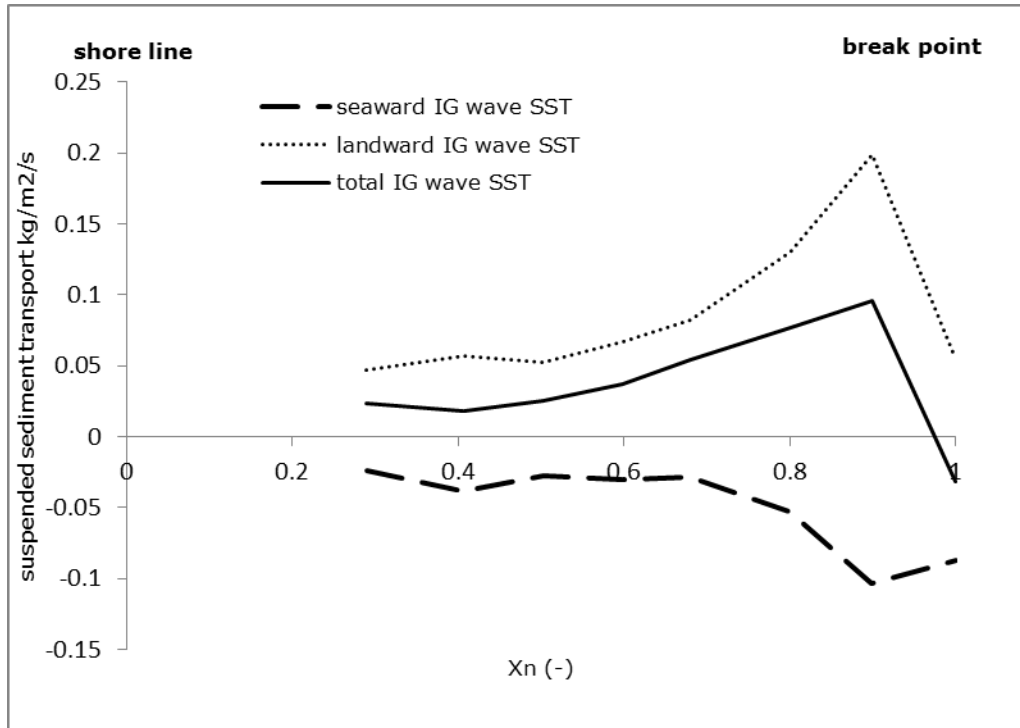
Figure 28, seaward, landward and total IG wave SST plotted against of average x_n per category x_c.

4.4   Wave envelope and inspection of the time series

To analyze which mechanisms were most likely responsible for the infragravity wave suspended transport pattern in the surf zone it was vital to quantify the modulation of gravity waves by infragravity waves. This to proved that mechanism involving modulation of gravity waves by infragravity waves can either be considered or rejected as dominant mechanism of SST by IG waves. As explained in section 3.3 the correlation between the SE or velocity wave envelope with the IG frequency filtered SSE or velocity time series is a measure of the modulation of gravity waves by IG waves. Figure 29 shows the correlation between the IG frequency filtered velocity time series (u_{IG}) and both the gravity wave envelope (SSE_{ENV}) and gravity velocity envelope (u_{ENV}). Figure 30 shows the correlation between the IG frequency filtered SSE time series (u_{IG}) and both the gravity wave envelope (SSE_{ENV}) and gravity velocity envelope (u_{ENV}).

Based on the four correlations per category as a function average x_n per category, the surf zone was separated into three sections :

- Section 1: for $x_n > 0.9$ negative correlation values were found. U_{IG} showed a negative correlation with u_{ENV} and SSE_{ENV} , correlation values measuring -0.10 and -0.20 respectively. But also SSE_{IG} showed a negative correlation with u_{ENV} and SSE_{ENV} , with correlation values of -0.23 and -0.19 respectively. The IG wave velocity and SSE both modulated the height of gravity velocity and SSE to be higher during of an IG wave through.

- Section 2: when $0.5 > x_n < 0.9$ small correlations were found, except for the SSE_{IG} and u_{ENV}, they prove to be positively correlated by a value of ~0.2. Meaning the IG wave SSE modulated the height of gravity velocity. The gravity wave velocity was higher during the passing of the crest of the wave.

- Section 3: when $x_n < 0.5$ increasing positive correlation were found between U_{IG} and both u_{ENV} and SSE_{ENV} up to 0.34 and 0.43 respectively at $x_n = 0.3$. In this region the IG wave velocity modulated both the gravity wave velocity and SSE. During the landward directed IG velocity phase, the gravity wave velocity and SSE was significantly larger compared to the seaward directed IG velocity phase. SSE_{IG} and u_{ENV} were also still positively correlated by a value of ~0.3.
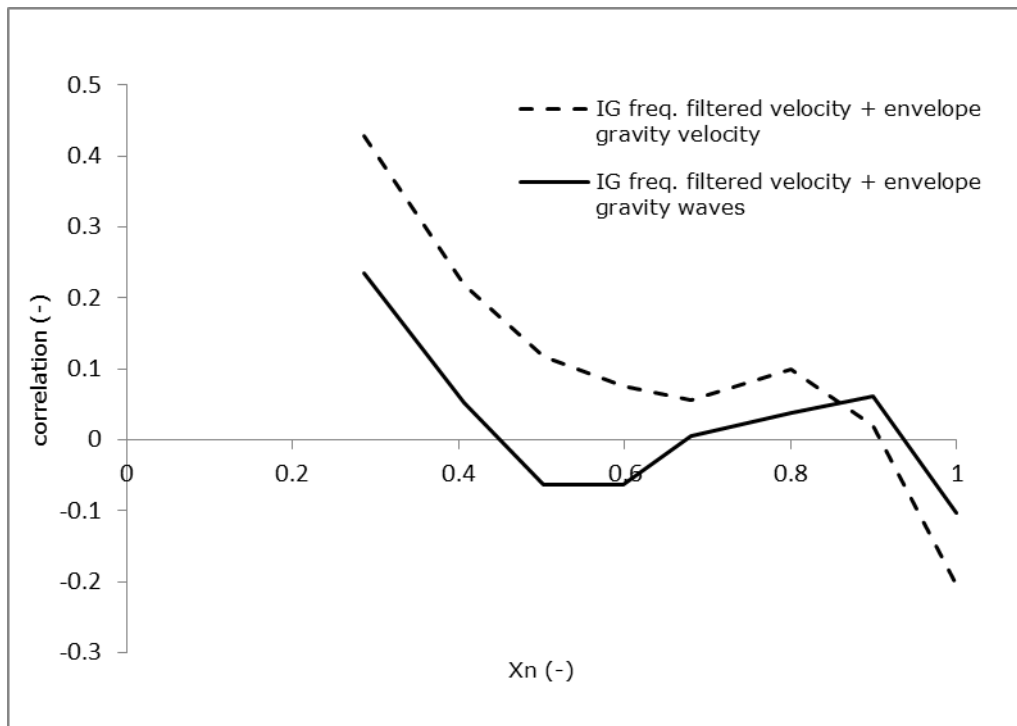
Figure 29, broken line indicates correlation between IG frequency filtered velocity and the gravity velocity envelope as a function of average x_n per category x_c. solid line shows correlation between IG frequency filtered velocity and the gravity wave envelope as a function of average x_n per category x_c.
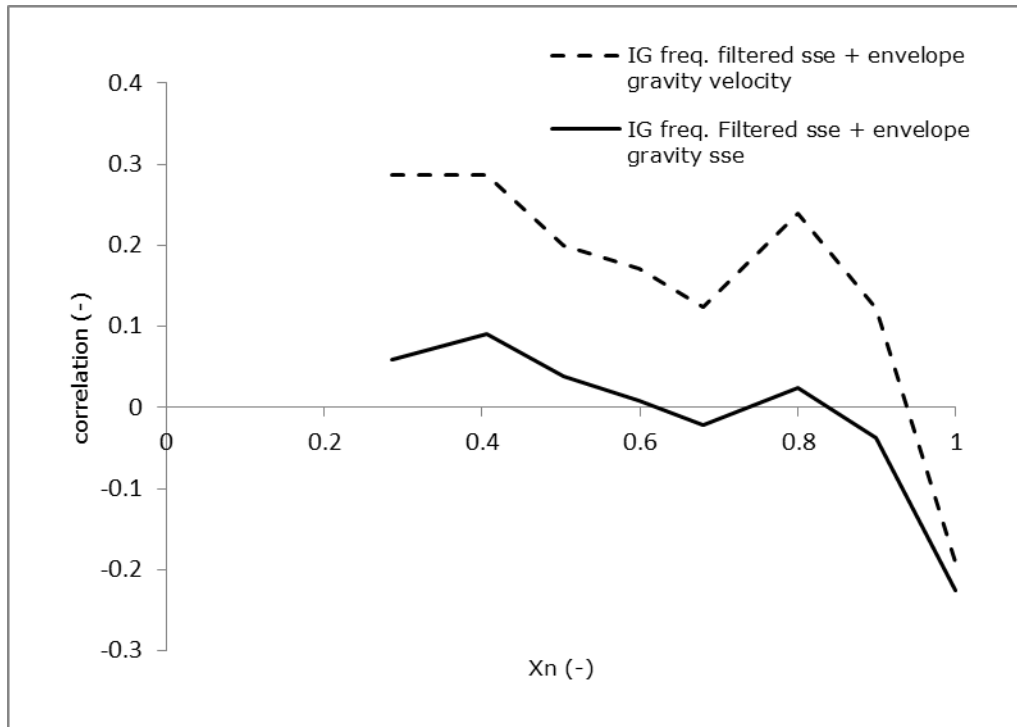
Figure 30, broken line indicates correlation between IG frequency filtered SSE and the gravity velocity envelope as a function of average x_n per category x_c. solid line shows correlation between IG frequency filtered SSE and the gravity wave envelope as a function of average x_n per category x_c.

The time series of SSE, velocity, SSC and SST are visually inspected for the sections $x_n > 0.9$, $0.5 > x_n < 0.9$ and $x_n < 0.5$. In figure 31,32 and 33 time series are showed for the different sections; were SSE is plotted in A, the total and IG frequency filtered cross-shore velocity are shown in B, total SSC and SST are plotted in C and in D the IG, gravity and mean SST are plotted. Time series for the three section of the surf zone were characterized as follows:

- Section 1: In figure 31 time series are shown measured on 3 October between 21.30 and 22.00. For this burst the x_n value was 1, h equalled 1.05 m, H_{off} was 0.98 m and the instrument height for both the EMF and the OBS was 19 cm. Individual peaks in SSC were associated with gravity waves. The peaks were however predominantly occurring during the seaward directed IG velocity phases, indicated with I, III and V. During the landward directed IG velocity phases II, IV and V, less sediment was suspended. The IG SST is also larger during the seaward IG velocity phases compared to the landward directed IG velocity phase. This was consistent with the negative IG wave SST at $x_n = 1$ in figure 28.
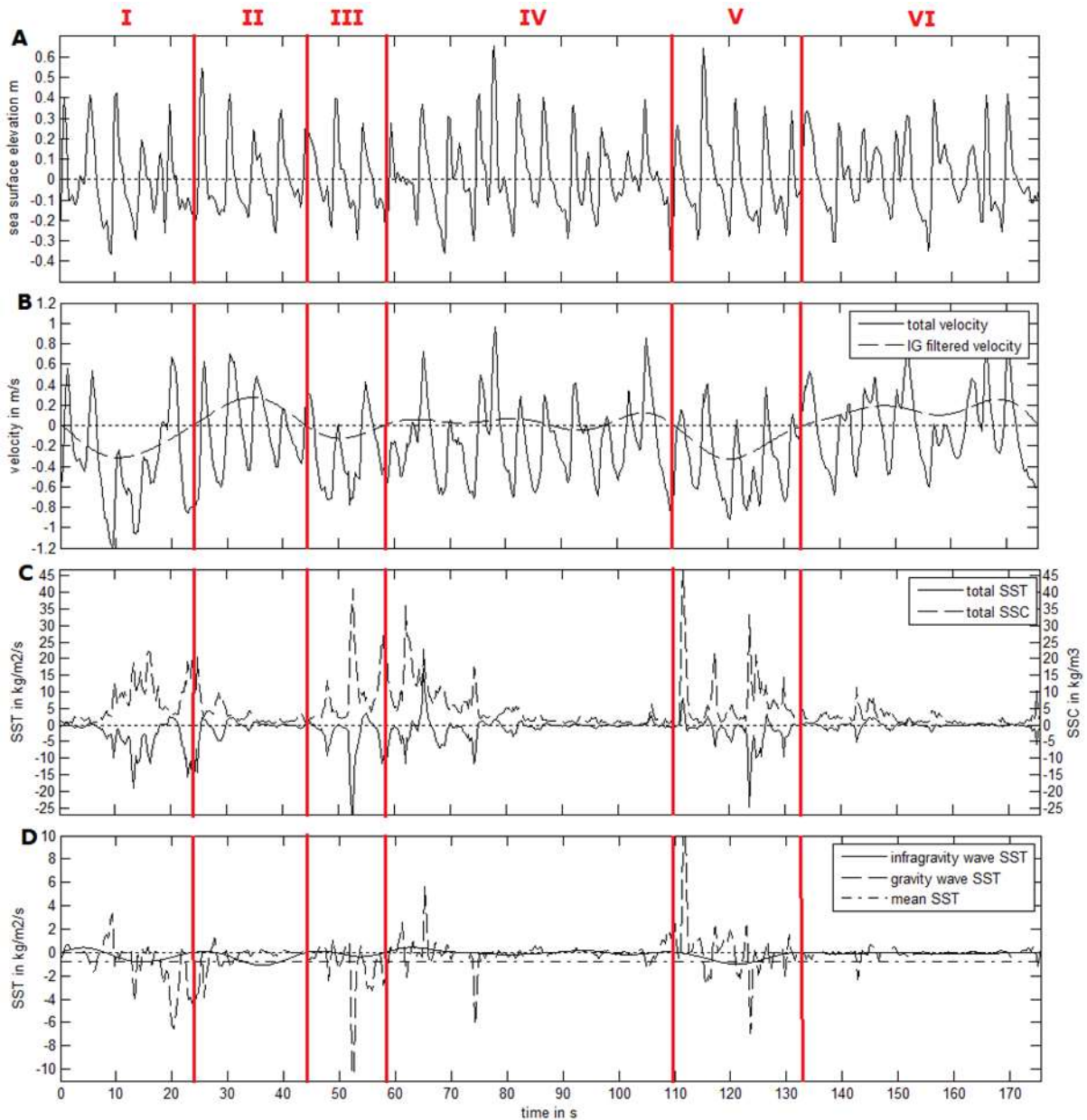
Figure 31, time series measured on 3 October between 21.30 and 22.00. In A the SSE, in B the total and IG frequency filtered cross-shore velocity , in C total SSC and SST and in D the IG, gravity and mean SST are plotted over time.

- Section 2: figure 32 shows time series measured on 6 October between 4.00 and 4.30. For this burst x_n equalled 0.81, h was 0.96 m, H_{off} was 2.24 m and the instrument height for both the EMF and the OBS was 18 cm. For these time series individual peaks in SSC also related to the passing of gravity waves. The peaks were however not only restricted to the seaward or landward directed IG velocity phases. The sediment was suspended during the seaward directed IG velocity phases (I, III,V and VII) and during the landward directed IG velocity phases (II, IV,VI and VIII), resulting in seaward and landward directed IG SST.
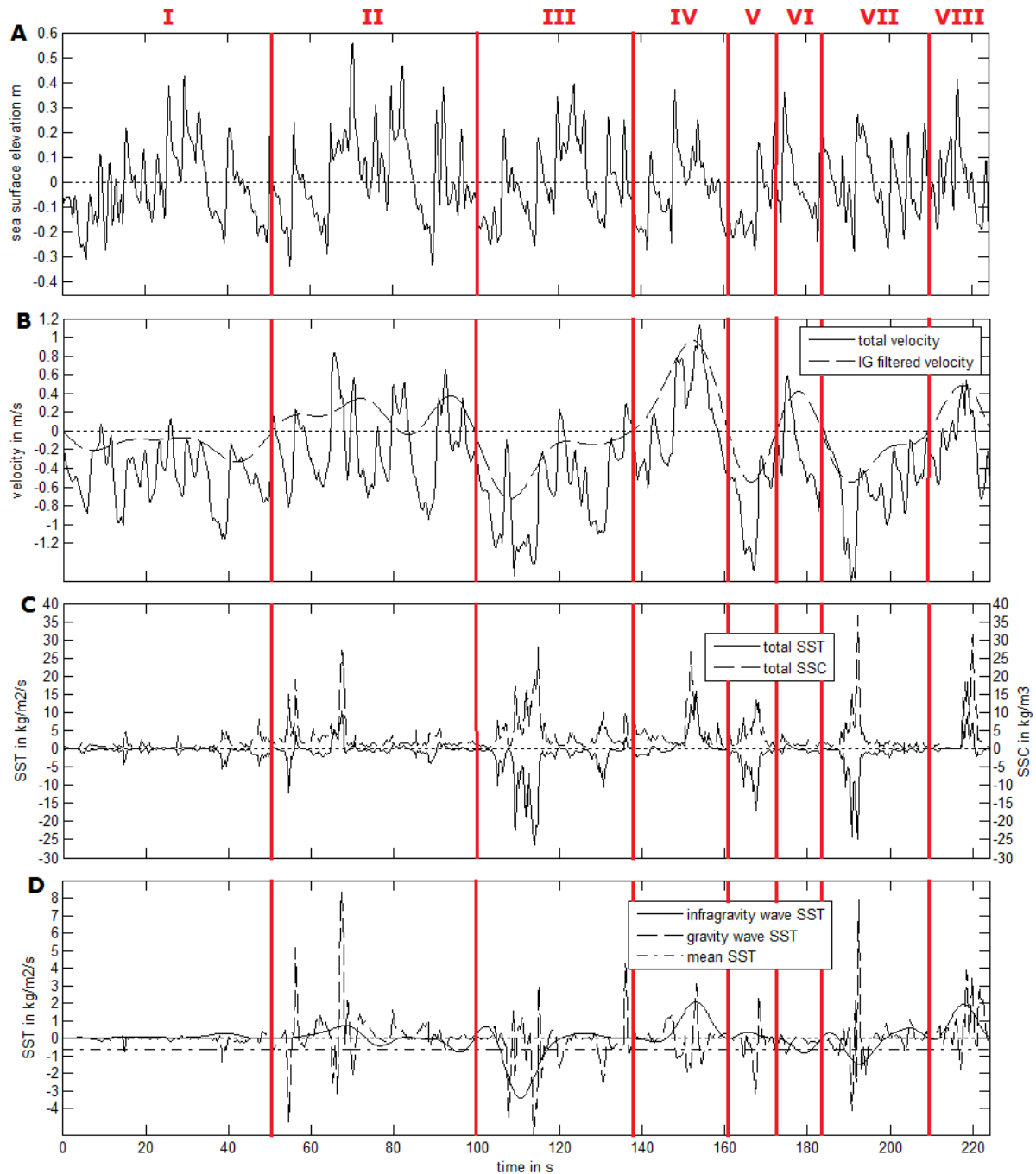
Figure 32, time series measured on 6 October between 4.00 and 4.30. In A the SSE, in B the total and IG frequency filtered cross-shore velocity , in C total SSC and SST and in D the IG, gravity and mean SST are plotted over time.

- Section 3: the time series shown in figure 33 are recorded on 7 October between 6.15 and 6.45. The x_n value for this burst was 0.43, h equalled 0.93 m, H_{off} was 2.26 m and the instrument height for both the EMF and the OBS was 11.8 cm. As for section 2 the peaks SSC were both occurring on seaward and landward directed IG velocity phases, the SSC pattern was however different. In figure 32, period I and V and VII show the seaward directed IG velocity phases.

For these periods the velocity and SSE record were largely dominated by IG waves. This is consistent with earlier finding, for in this section the IG_{imp} was proved to be high (figure 23). Especially for period I and V individual gravity bores were hard to recognize in both the SSE and velocity record. It seems that gravity bores were unable to propagate through the large opposing IG velocity. During period I and VII sediment was suspended continuously for a large part of the IG velocity phase and the highest SSC can be observed when the negative velocity is at a maximum. This suggests that sediment was suspended by IG waves. The SSC pattern for the landward directed IG velocity phases was generally different compared to the SSC pattern for the seaward directed IG velocity. The largest peaks in SSC occur just after flow reversal, when the total velocities increased rapidly and the water level rose fast. For periods VI and VIII large suspension events just happened just after flow reversal. This suggests that the gravity bores that could not propagate through the large opposing IG velocity were released just after flow leading to a large peak in velocity. The landward directed peak in velocity coincided with a large peaks in SSC, resulting in landward IG wave SST.
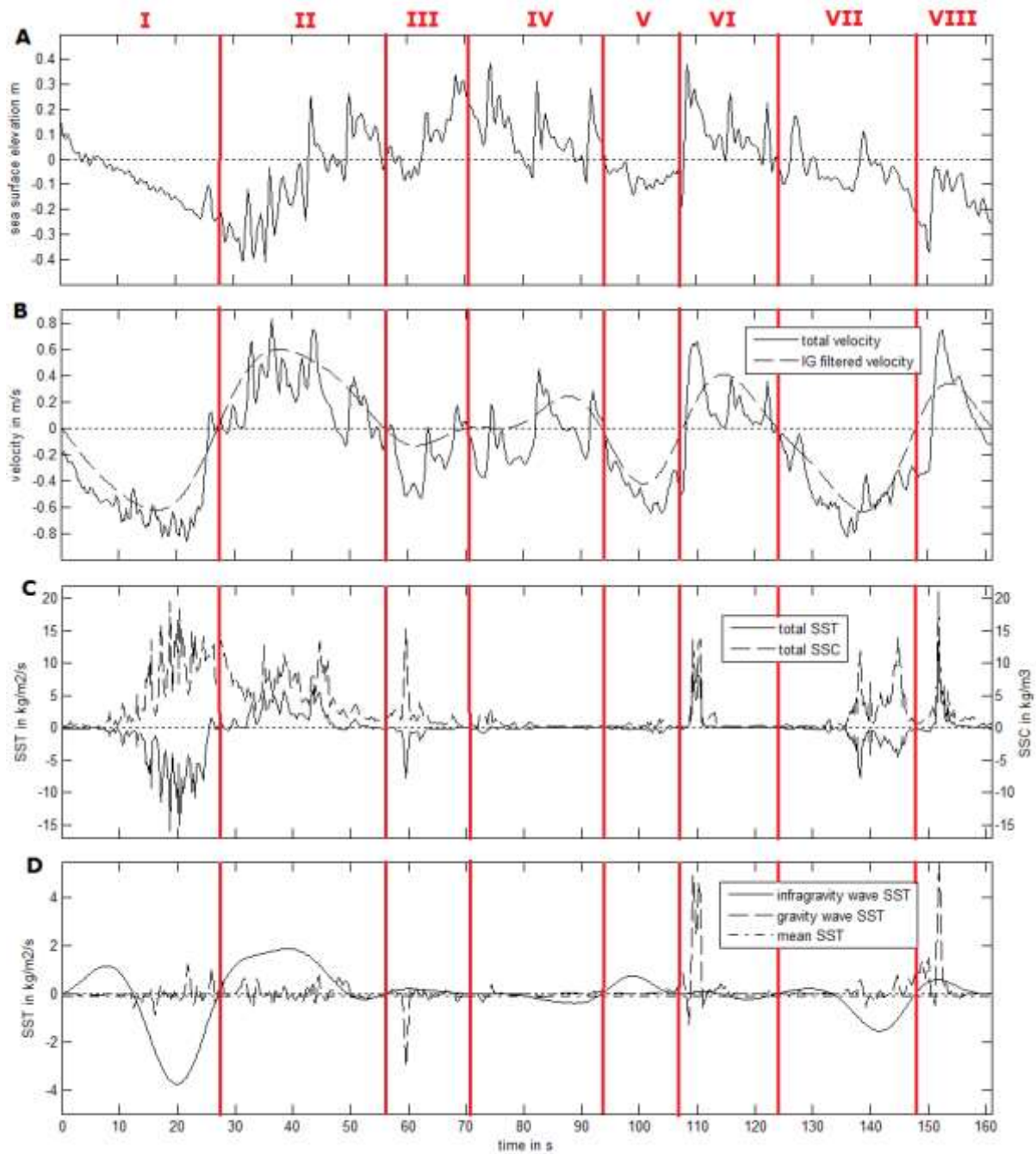
Figure 33, time series measured on 7 October between 6.15 and 6.45. In A the SSE, in B the total and IG frequency filtered cross-shore velocity , in C total SSC and SST and in D the IG, gravity and mean SST are plotted over time.

5 Discussion

The inaccuracies and limitations of the research method used are discussed with respect to x_n, IG_{imp} and SST. The SST fluxes were calculated per burst using only the instantaneous SSC of the lowermost OBS sensor and velocity on one height above the bed. Hence the SST fluxes are not the true transports, they are the SST fluxes at one point in the water column close to the bed. To avoid calculating the depth integrated SST flux, with limited sensors and an unknown location of the boundary layer, SST fluxes close to the bed were considered to be a reasonable estimate of the actual mean SST flux for the whole water column. More accurate would be to calculate the depth integrated SST flux with the use of a vertical array of collocated OBS and EMF sensors per tripod.

The position of the senores above the bed was not constant. Large part of the period the profile and the instruments were not inundated and thus morphological inactive. Observations of the mini-frame data also shows that burial of the lower OBS could occur in half an hour, meaning at least 10 cm of vertical sedimentation in short notice. Even within the inundation period sedimentation was non-linear. This means that there was a large inaccuracy of when profiles heights and instrument heights were interpolated linearly over a period of two or more tidal periods.

The breakpoint was determined based on the location of the largest dissipation. When the largest dissipation value was found at the most seaward station, this location was assumed to be the breaking location. In fact the actual breakpoint could be located further seaward. Also the breakpoint location were restricted to locations of measuring stations. The fieldwork area wasrecorded in imagery data set collected at the ARGUS "COAST-3D" video-tower. It could have been more accurate to use this imagery data to derive a break point of waves. Waves don't break on one location, but over a large area in the surf zone, the breaker zone. Break point should be interpreted the point where most waves break. Furthermore it was visually confirmed that waves reformed in the trough after breaking on the intertidal bar. This was also confirmed by local dissipation maxima between the largest dissipation value and the shore line.

The determination of the coast line location was also influenced by inaccuracies in the instrument height and profile height. Water depth and thus the mean sea level was influenced by the instrument height, so the location of intersection between the mean sea level and the bottom profile was underestimated or overestimated. Sensors that also measure the instrument height over time could have provided better accuracy for the determination of x_s. Both the determination of x_s and x_b cause inaccuracies in the x_n variable.

The IG_{imp} was strongly related to the x_n. Also H_{off} showed a less significant relation with IG_{imp}. IG_{imp} might have been better explained using a combined parameter of x_n and H_{off}. Another option would have been to analyse the relationship of x_n and IG_{imp} for different H_{off} scenarios. Especially a cut-off for $H_{off} = 1m$ was justified, for this was regarded as the boundary between calm and storm conditions in chapter 4.1 and 4.2. Limitation is that only 11.4 % of the bursts had an H_{off} value of lower than 1 m.

The last research question, considering the mechanisms most likely responsible for the infragravity wave suspended transport pattern in the surf zone, is not answered yet. Based on pattern of IG frequency SST as a function of x_n, inspection of SSE, velocity and SST time series and modulation of gravity waves by infragravity waves, a theory was formulated. As part theory the three earlier defined sections of the surf zone were considered. In figure 34 two graphs are shown adjusted from figure 22 and 29. In 34A IG_{imp} is plotted against x_n for all bursts (indicated with the small crosses), with a linear trend line based on all data, black dots indicating the average IG_{imp} per category of x_n. Error bars indicated the standard error per category. In 34B the correlation between the IG frequency filtered velocity time series (u_{IG}) and the gravity wave envelope (SSE_{ENV}) and gravity velocity envelope (u_{ENV}) is shown. In both figures the sections of the surf zone are indicated. In figure 34 A the IG wave SST mechanisms associated with the sections are indicated. In figure 34 B the type of modulation is indicated per section. The IG wave SST was characterized per section as follows:

- Section 1: for $x_n > 0.9$, the IG wave SST was offshore directed (figure 27). Time series analysis shows that peaks in SSC were associated with gravity waves, with the peaks predominantly occurring during the seaward directed IG velocity phases. Less sediment was suspended during the seaward IG velocity phases. This section was also characterized by negative modulation and the IG_{imp} has a value of 0.2 – 0.3. Concluded was that mechanism 2 is most likely responsible for the IG wave SST in this section.

- Section 2: for $0.5 > x_n < 0.9$, the IG wave SST was landward directed, decreasing in magnitude landward. The pattern q_{IG} as a function of x_n showed great resemblance with the pattern described by the advection mechanism (Aagaard & Greenwood, 2008). In this section no modulation of gravity waves by IG waves was observed. The time series showed that the sediment was suspended during the seaward directed IG velocity phases and during the landward directed IG velocity phases, resulting in seaward and landward directed IG SST. The IG SST values per burst, for x_n values between 0.5 and 0.9, suggested that that the positive transport by IG is larger, this was however hard to confirm with the inspection of time series. Although mechanism 1 is the only mechanism consistent with the IG wave SST pattern and no modulation occurred, confirmation from time series analysis was impossible.

- Section 3: when $x_n < 0.5$, time series in figure 33 showed the velocity and SSE record were largely dominated by IG waves. Also from figure 34B. For this section IG_{imp} was larger compared to the other sections. This section was also characterized by positive modulation of gravity waves and velocity by IG wave velocity. During the seaward directed IG wave velocity phases, individual gravity bores were hard to recognize in both the SSE and velocity record. Gravity bores were unable to propagate through the large opposing IG velocity. In section 3 sediment was predominantly suspended continuously for a large part of the seaward directed IG velocity phase. The highest SSC were observed when the negative velocity is at a maximum. This suggests that sediment was suspended by IG waves and is consistent with mechanism 4. During the landward directed IG velocity phase time series analysis showed that the largest peaks in SSC occurred just after flow reversal, when the total velocities increased rapidly and the water level rose fast. The gravity bores counteracted by opposing IG velocity, were released just after flow reversal leading to a large peak in velocity. IG wave SST during the landward directed IG velocity phases was consistent with mechanism 5. The large peaks in velocity after flow reversal and small gravity waves in the seaward directed velocity phase were also consistent with the positive modulation of gravity waves and velocity by IG velocity in this section (figure 34B). No analysis on skewness was performed, but the positive modulation could also point to mechanism 3. Sediment is not necessarily suspended by the largest IG waves but by a large peak in velocity after flow reversal. It seems positive modulation occurred but time series are more compatible with mechanism 5.

Figure 34 A, IG$_{imp}$ is plotted against x$_n$, the crosses indicate the values for all bursts. Black dots indicate the average IG$_{imp}$ per category of x$_n$ with the coinciding error bars indicating the standard error per category. The linear trend line based on all data points is indicated with a line. The three defined sections of the surf zone are indicated in red. The breakpoint, shoreline and the different mechanisms per section are also indicated. B, indicates correlation between IG frequency filtered velocity and the gravity velocity envelope (broken line) and the gravity wave envelope (solid line), as a function of average x$_n$ per category x$_c$. where the red lines show the boundaries between the three defined sections of the surf zone. Type of modulation is also indicated for the three sections.

6 Conclusion

The IG_{imp} was related to x_n with a R^2 of 0.5271. IG_{imp} increases towards the coast line with a value of ~0.25 at breaking point ($x_n =1$) up to ~0.55 close to shore at $x_n =0.3$. Hoff and h were less significantly related to IG_{imp} compared to x_n, with R^2 values 0.2586 and 0.0939 respectively.

The IG wave SST was analysed as a function of x_n. IG wave SST was mainly directed landward, except for $x_n > 0.9$, seaward transport occurred. For $x_n = 0.9$ the maximum IG wave SST was calculated, decreasing in magnitude towards the coast line. The IG wave SST was comparable in magnitude with the landward directed gravity wave SST. In most of the surf zone, the seaward directed mean SST component is dominant. At $x_n = 0.9$, the mean SST was even ~7 larger than the IG wave SST. In most of the surf zone the total SST was therefore seaward directed. This was consistent with morphological changes of the profile during storm conditions (88.6% of the bursts were collected during storm conditions). Only close to shore, $x_n = 0.3$, the gravity and IG SST were comparable with the mean component leading to positive total SST.

Based on the IG wave SST, type of modulation and inspection of the time series, three sections within the surf zone were defined:

- Section 1: for $x_n > 0.9$, was characterized by negative modulation and small $IG_{imp.}$ Time series analysis shows that peaks in SSC generated by gravity waves, predominantly occurred during the seaward directed IG velocity phases. This resulted in negative IG wave SST. Concluded is that mechanism 2 was most likely responsible for the IG wave SST in this section.
- Section 2: for $0.5 > x_n < 0.9$ no modulation was present. IG wave SST was landward directed, decreasing in magnitude landward as a function of x_n. This pattern was comparable with the pattern described by the advection mechanism, mechanism 1. Although mechanism 1 was the only mechanism consistent with the IG wave SST pattern, time series could not prove the occurrence of the advection mechanism.

- Section 3: when $x_n < 0.5$, was characterized by landward increasing of positive modulation of gravity waves and velocity by IG wave velocity. Also the IG_{imp} was higher compared to the other sections and increased landward. During the seaward directed IG wave velocity phases, gravity waves were small and sediment is predominantly suspended continuously for a large part of the seaward directed IG velocity phase. The SST by IG waves was seaward directed and consistent with mechanism 4. During the landward directed IG velocity phase time series analysis showed that the largest peaks in SSC occur just after flow reversal. IG wave SST during the landward directed IG velocity phases was consistent with mechanism 5. The large peaks in velocity after flow reversal and small gravity waves in the seaward directed velocity phase were consistent with the positive modulation.

List of Figures

References

Aagaard , T., Kroon, A., Anderson, S., Sørensen, R. M., Quartel, S., Vinther, N. (2005). Intertidal beach change during storm conditions; Egmond, The Netherlands. *Marine Geology*, 218 pp. 65-80.

Aagaard, T., Greenwood , B. (1994). Suspended sediment transport and the role of infragravity waves in a barred surf zone. *Marine Geology*, 118 pp. 23-48.

Aagaard, T., Greenwood , B. (1995b). Longshore and cross-shore suspended sediment transport at far infragravity frequencies in a bar environment. *Continental Shelf Research*, Vol. 15 No.10 pp. 1235-1249.

Aagaard, T., Greenwood, B. (1995a). Suspended sediment transport and morphological response on a dissipative beach. *Continental Shelf Research*, Vol. 15 No.9 pp. 1061-1086.

Aagaard, T., Greenwood, B. (2008). Infragravity wave contribution to surf zone sediment transport - the role of advection. *Marine Geology*, 251 pp.1-14.

Aagaard, T., Hughes, M. G. (2010). Breaker turbulence and sediment suspension in the surf zone. *Marine Geology*, 271 pp. 250-259.

Aagaard, T., Black, K. P., Greenwood, B. (2002). Cross-shore suspended sediment transport in the surf zone: a field-based parameterization. *Marine Geology*, 185 pp. 283-302.

Aagaard, T., Hughes, M. G., Møller-Sørensen, R., Anderson, S. (2006). Hydrodynamics and sediment fluxes across an onshore migrating intertidal bar. *Journal of Coastal Research*, 22(2) pp. 247-259.

Alsina, J. M., Cáceres, C. (2011). Sediment suspension events in the inner surf and swash zone. Measurements in large-scale and high-energy wave conditions. *Ocean Engineering*, 58 pp. 657-670.

Bagnold, R. A. (1956). The flow of cohesionless grains in fluids. *Royal Society London*, Ser. B 249 pp. 235-297.

Baldock, T. E., Alsina, J. A., Cáceres, I., Vicinanza, D., Contestabile, P., Power, H., et al. (2011). Large-scale experiments on beach profile evolution and surf and swash zone sediment transport induced by long waves, wave groups and random waves . *Coastal Engineering*, 58 pp. 214-227.

Baldock, T. E., Manoonvoravong, P., Pham, Kim Son. (2010). Sediment transport and beach morphodynamics induced by free long waves, bound long waves and wave groups. *Coastal Engineering*, 57 pp. 898-916.

Beach, R. A., Sternberg, R. W. (1988). Suspended Sediment transport in the surf zone: response to cross-shore infragravity motion. *Marine Geology*, 80 pp. 61-79.

Beach, R. A., Sternberg, R. W. (1996). Suspended sediment transport in the surf zone: response to breaking waves. *Continental Shelf Research*, Vol. 16 No. 15 pp. 1989-2003.

Butt , T., Russell, P. (1999). Suspended sediment transport mechanisms in high energy swash. *Marine Geology*, 161 pp. 361-375.

Butt, T., Russell, P., Puleo , J., Miles, J., Masselink, G. (2004). Influence of bore turbulence on sediment transport in swash and inner surf zones. *Continental Shelf Research*, 24 pp. 757-771 .

Butt, T., Tinker, J., Masselink , G., O'Hara, T., Russell, P. (2009). Field observations of sediment fluxes in the inner-surf and swash zone. *Journal of Coastal Research*, 25(4) pp. 991-1001.

Deigaard, R., Jakobsen, J. B., Fredsøe, J. (1999). Net sediment transport under wave groups and bound long waves. *Journal of Geophysical Research*, vol. 104 No. C613 pp. 559-575.

Doering, J. C., Bowen, A. J. (1995). Parametrization of orbital velocity asymmetries of shoaling and breaking waves using bispectral analysis. *Coastal Engineering*, 26 pp. 15-33.

Guza, R. T., Inman, D. (1975). Edge waves and beach cusps. *Journal Geophysical Research*, vol. 80 pp. 2997-3012.

Houser, C., Greenwood, B. (2005). Hydrodynamics and sediment transport within the inner surf zone of a lacustrine mulitple-barred nearshore. *Marine Geology*, 218 pp. 37-63.

Houser, C., Greenwood, B. (2007). Onshore migration of a swash bar during a storm. *Journal of Coastal Research*, 23 pp.1-14.

Longo, S., Petti, M., Losada, I. J. (2002). Turbulence in the swash and surf zones: a review. *Coastal Engineering*, 45 pp. 129-147.

Longuet-Higgins, M. S., Stewart, R. W. (1962). Radiation stress and mass transport in gravity waves, with application to 'surf beats'. *Journal of Fluid Mechanics*, 13 pp. 481-504.

Mariño-Tapia, J., Russell, P. E., O'Hara, T. J., Davidson, M. A., Huntley, D. A. (2007a). Cross-shore sediment transport on natural beaches and its relation to sandbar migration patterns: 1. Field observations and derivation of a transport parametrization. *Journal of Geophysical Research*, vol. 12 C03002 doi:10.1029/2005JC002893.

Mariño-Tapia, J., Russell, P. E., O'Hara, T. J., Davidson, M. A., Huntley, D. A. (2007b). Cross-shore sediment transport on natural beaches and its relation to sandbar migration patterns: 2. Application of the field transport parametrization. *Journal of Geophysical Research*, vol.12 C03002 doi:10.1029/2005JC002894.

Masselink, G., Evans, D., Hughes, M. G., Russell, P. (2005). Suspended sediment transport in the swash zone of a dissipative beach. *Marine Geology*, 216 pp. 169-189.

Munk, W. H. (1949). Surf beats. *Transactions of the American Geophysical Union*, 30 pp. 849-854.

Nielsen, P. (2002). Coastal bottom boundary layers and sediment transport. *Advanced Series of Coastal Engineering*, Vol. 4 World Scientific Singapore pp.324.

O'Hara, T. J., Huntley, D. A. (1994). Bar formation due to wave groups and associated long waves. Marine Geology. *Marine Geology*, 116 pp. 313-325.

Osbourne, P. D., Greenwood, B. (1992a). Frequency dependant cross-shore suspended sediment transport. 1. A non-barred shoreface. *Marine Geology*, 106 pp.1-24.

Osbourne, P. D., Greenwood, B. (1992b). Frequency dependent cross-shore suspended sediment transport. 2. A barred shoreface. *Marine Geology*, 106 pp. 25-51.

Petti, M., Longo , S. (2001). Turbulence experiments in the swash zone. *Coastal Engineering*, Vol. 43 Issue 1 pp. 1-24.

Price, T. D., Ruessink, B. G. (2008). Morphodynamic zone variability on a microtidal barred beach. *Marine Geology*, Vol. 251 pp. 98-109.

Roelvink, J. A., Brøker, I. (1993). Cross-shore profile models. *Coastal Engineering*, 21 pp. 163-191.

Ruessink , B. G., Houwman, K. T., Hoekstra, P. (1998). The systematic contribution of transporting mechanisms to the cross-shore sediment transport in water depths of 3 to 9 m. *Marine Geology*, 152 pp. 295-324.

Russell, P. E. (1993). Mechanisms for beach erosion during storms. *Continental Shelf Research*, Vol. 13 No 11 pp. 1243-1265.

Schoonees, J. S., Theron, A. K. (1995). Evaluation of 10 cross-shore sediment transport/morphological models. *Coastal Engineering*, 25 pp. 1-41.

Smith, G. G., Mocke, G. P. (2002). Interaction between breaking/broken waves and infragravity-scale phenomena to control sediment suspension transport in the surf zone. *Marine Geology*, 187 pp. 329-345.

Symonds, G., Huntley, D. A., Bowen, A. J. (1982). Two-Dimensional Surf Beat: Long Wave Generation by a Time-varying Breakpoint. *Journal of Geophysical Research*, Vol. 85 No. C1 pp. 492-498.

Tinker, J., O'Hara, T., Masselink, G., Butt, T., Russell , P. (2009). A cross-shore suspended sediment transport shape function parameterization for natural beaches. *Continental Shelf Research*, 29 pp. 1948-1960.

Van Rijn, L. C., Ruessink, B. G., Mulder, J. P. (2002). *Coast3D-Egmond. The behaviour of a straight sandy coast on the time scale of storms and seasons.* Amsterdam: Aqua Publications.

Voulgaris, G., Collins, M. B. (2000). Sediment resuspension on beaches: response to breaking waves. *Marine Geology*, 167 pp. 167-187.

Yu, Y., Sternberg, R. W., Beach, R. A. (1993). Kinematics of breaking waves and associated suspended sediment in the nearshore zone. *Continental Shelf Research*, Vol. 13 No. 11 pp. 1219-1242.